IMPLEMENTATION OF THE CRYSTAL PLASTICITY FINITE ELEMENT METHOD

by

Mehrdad Ghanbari Azar

B.S., Mechanical Engineering, Tabriz University, 2014

Submitted to the Institute for Graduate Studies in
Science and Engineering in partial fulfillment of
the requirements for the degree of
Master of Science

Graduate Program in Mechanical Engineering

Boğaziçi University

2018

IMPLEMENTATION OF THE CRYSTAL PLASTICITY FINITE ELEMENT METHOD

APPROVED BY:

Assoc. Prof. C.Can Aydıner (Thesis Supervisor) .....

Prof. Dr. Fazıl Önder Sönmez .....

Assist. Prof. Eralp Demir .....

DATE OF APPROVAL: 03.08.2018

ACKNOWLEDGEMENTS

I would like to express my deep gratitude to my thesis supervisors Prof. Jeremy Kyle Mason and Prof. C.Can Aydıner, for their patient guidance, enthusiastic encouragement and useful critiques for this work. I am also grateful to Prof. Eralp Demir and Prof. Fazıl Önder Sönmez for taking time to be on my thesis committee.

I am extremely grateful to my family, Seifali Ghanbari Azar, Shiva Azizi, Arad Ghanbari Azar and Valeh Ghanbari Azar, for giving me freedom in my decisions and believing me and teaching me to dream big and bigger, and for their endless support and keeping me inspired and motivated throughout my life and especially during my M.Sc program.

There have been many people who have walked alongside me during the last years, They have guided me, placed opportunities in front of me and showed me the doors that might be useful to open, I would like to thank them all, particularly, my Dear friends, Soheil, Sina, Koorosh, Eren and Gülcan for always being there for me and sharing great moments with me. I would like to extend my deepest thanks to my dear Mona who helped me to see the light at the end of tunnel and for her lovely spirit and constant support.

This work was in part supported by the Scientific and Technological Research Council of Turkey (TÜBİTAK).

ABSTRACT

IMPLEMENTATION OF THE CRYSTAL PLASTICITY FINITE ELEMENT METHOD

Computational materials science is one of the fastest growing areas in modern materials research, and controlling the microstructure of a polycrystal is crucial to designing advanced materials. The extreme environments often used in industrial forming operations are not suitable for modern microscopy techniques though, encouraging the use of simulations to investigate the mechanisms involved.

Different physics-based models such as crystal plasticity theories have shown the ability to predict the mechanical response of materials during plastic deformation. Since classical constitutive laws are strongly simplified, they are neither able to accurately predict crystallographic texture and its evolution, (the main source of the anisotropy in crystals) nor account for grain size effects. More modern crystal plasticity finite element methods address some of these issues using strain gradient theories and constitutive relations based on dislocation densities.

The key factor that makes the finite element method preferred for crystal plasticity is the ability to handle the complicated internal and external boundary conditions that are characteristic of plastic deformation. The current work is focused on simulations of crystal plasticity on the single crystal scale and below using the finite element method.

ÖZET

KRİSTAL PLASTİSITE SONLU ELEMANLARIN UYGULAMASI

Hesaplamalı malzeme bilimi, modern malzeme araştırmalarında en hızlı büyüyen alanlardan biridir ve bir polikristalin mikroyapısını kontrol etmek ve gelişmiş materyallerin tasarlanması için çok önemlidir.

Endüstriyel şekillendirme işlemlerinde sıklıkla kullanılan özel ortamlar, modern mikroskopi teknikleri için uygun olmamakla birlikte, söz konusu mekanizmaları araştırmak için simülasyonların kullanılmasını teşvik etmektedir.

Kristal plastisite teorileri gibi farklı fizik tabanlı modeller, plastik deformasyon sırasında malzemelerin mekanik tepkisini tahmin etme kabiliyetini göstermiştir. Klasik kurucu yasalar güçlü bir şekilde basitleştirildiği için, kristalografik dokuyu ve onun evrimini (kristallerde anizotropinin ana kaynağı) doğru bir şekilde tahmin edemedikleri gibi, tahıl boyutu etkilerini de hesaba katmazlar. Daha modern kristal plastisite sonlu elemanlar metotları, bu sorunların bir kısmını, gerilme gradyan teorilerini ve dislokasyon yoğunluklarına dayanan kurucu ilişkileri kullanarak ele almaktadır.

sonlu elemanlar yönteminin kristal plastisite alanında tercih edilmesinin en önemli faktörü, plastik deformasyonun karakteristiği olan karmaşık iç ve dış sınır koşullarını ele alma becerisidir. Mevcut çalışma, sonlu elemanlar yöntemi kullanılarak tek kristal ölçeklerinde kristal plastisite simülasyonlarına odaklanmıştır.

TABLE OF CONTENTS

ACKNOWLEDGEMENTS iii
ABSTRACT iv
ÖZET v
LIST OF FIGURES viii
LIST OF TABLES xii
LIST OF SYMBOLS xiii
LIST OF ACRONYMS/ABBREVIATIONS xv
1. INTRODUCTION 1
2. CRYSTAL PLASTICITY FINITE ELEMENT METHOD 3
2.1. Historical Review 3
2.2. Crystal Anisotropy 4
2.3. Crystal plasticity finite element method 6
2.3.1. Crystal plasticity models 9
2.3.2. Schmid's law 10
2.4. Flow Kinematics and constitutive relations 11
2.5. Crystal plasticity Fast Fourier Transform Method 15
3. PROCEDURE AND RESULTS 18
3.1. Viscoelasto-plastic deformation model (Kalidindi's method and results) 19
3.2. Viscoelasto-plastic deformation model (Marin and Dawson's method and results) 24
3.2.1. Investigating the Effect of Number of Elements in Stress Relaxation Tests 31
3.2.2. Investigating the Effect of Number of Time Steps in Stress Relaxation Tests 36
3.2.3. Investigating the Effect of Compression direction on Deformation in Stress Relaxation Test 37
3.2.4. Polycrystal Modelling for the Relaxation Test 40
3.2.5. Reverse Loading Modelling 44
3.2.6. Polycrystal Modelling for the Reverse Loading Test 47

3.3. Viscoelasto-plastic deformation model (Cuitino and Ortiz's method) . . 52
4. CONCLUSION 56
5. RECOMMENDATIONS FOR FUTURE WORK 57
REFERENCES 58

LIST OF FIGURES

Figure 2.1. Comparison between earing in Aluminum can after cup-drawing: (a) CPFEM simulation (b) experiment [62] 5

Figure 2.2. Four commonly used homogenization schemes. Reproduced from [61]. 7

Figure 2.3. Components of CPFEM modelling for a case with multiple deformation mechanisms (dislocation and twinning). [62] 9

Figure 2.4. Representation of Schmid factor for a sample under uniaxial tension. Reproduced from [16]. 10

Figure 2.5. Different illustrations of a sample. (a) Geometric model (b) partitioned model (c) partitioned mesh (reproduced from [65]). 12

Figure 2.6. Deformation gradient multiplicative decomposition into elastic and plastic parts. Reproduced from [43]. 13

Figure 2.7. Deformed configuration of the RVE from simulations after 40% thickness reduction. (a) FE (b) FFT. Reproduced from [59]. . . . 16

Figure 2.8. Results from rolling simulations. Top row: distribution of accumulated plastic strain. Bottom row: stress distribution. Left: FE. Right: FFT. Reproduced from [59]. 17

Figure 3.1. Illustration of a finite element mesh where four-node tetrahedral elements compose a cube. 19

Figure 3.2. Calculation scheme to determine $\boldsymbol{T}^*$ as a function of $\boldsymbol{F}$ [49]. . . . 20

Figure 3.3. Von-Mises - time plot of Kalidindi's time-integration procedure. . 24

Figure 3.4. Decomposition of deformation gradient into elastic and plastic parts [46]. 25

Figure 3.5. Four-noded tetrahedral element used for the simulations. 33

Figure 3.6. Initial condition and mesh of the sample with one element in each direction. 33

Figure 3.7. Final shape of the sample after the relaxation test with one element in each direction. 34

Figure 3.8. Initial condition and mesh of the sample with two elements in each direction. 35

Figure 3.9. Final shape of the sample after the relaxation test with two elements in each direction. 35

Figure 3.10. Comparison between different numbers of elements in normalized stress - time curve. 36

Figure 3.11. Comparison between different time steps for the normalized effective stress-time relation during the relaxation test for two elements along each axis. 37

Figure 3.12. Normalized effective stress - time relation during relaxation test for two elements along each axis, 150 total time steps, and compression along the $\langle 110 \rangle$ crystal direction. 38

Figure 3.13. Normalized effective stress - time relation during a relaxation test with two elements along each axis, 150 total time steps, and compression along the ⟨111⟩ direction. 39

Figure 3.14. Non-convergence of the volumetric part of the stress - time curve for a single crystal in the relaxation test. 39

Figure 3.15. Final shape of the relaxation test for a polycrystal with 40 crystals. 40

Figure 3.16. Pole figure representation of the initial crystal orientations for relaxation test. 41

Figure 3.17. Pole figure representation of the crystal orientations before the relaxation phase. 42

Figure 3.18. Normalized effective stress - time relation during a relaxation test for a polycrystal with 40 crystals and 150 total time steps. 43

Figure 3.19. Stress - time curve for a polycrystal during a relaxation test. Reproduced from [46]. 43

Figure 3.20. Final shape of the sample after the cyclic loading test for a single element in each direction. 45

Figure 3.21. Final shape of the sample after the reverse loading test for two elements in each direction. 45

Figure 3.22. Effect of the number of elements on the stress - strain curve in the cyclic loading test. 46

Figure 3.23. Non-convergence of the volumetric part of the stress - time curves of individual crystals in the reverse loading model. 47

Figure 3.24. Final shape of the sample after the reverse loading test for an aggregate with 40 crystals. 48

Figure 3.25. Pole figure representation of the initial crystal orientations for cyclic loading test. 49

Figure 3.26. Pole figure representation of the crystal orientations when the tension is reversed to compression in the cyclic loading test. 49

Figure 3.27. Pole figure representation of the crystal orientations when the compression is reversed to tension in the cyclic loading test. 50

Figure 3.28. Normalized effective stress - strain curve during reverse loading test for a polycrystal with two elements along each axis and 150 total time steps. 51

Figure 3.29. Stress - strain curve for the cyclic loading case. Reproduced from [46]. 51

LIST OF TABLES

Table 2.1. Slip directions $\boldsymbol{m}^\alpha$ and slip plane normals $\boldsymbol{n}^\alpha$ for an FCC crystal. . 11

Table 3.1. material parameters for annealed OFHC copper 24

Table 3.2. material parameters 32

LIST OF SYMBOLS

$\bar{\boldsymbol{A}}$	Fourth order Jacobian tensor
$\boldsymbol{B}$	Strain field interpolation matrix
C	Elasticity tensor
$\hat{\boldsymbol{C}}$	Tangential stiffness matrix
$\boldsymbol{C}^e$	Right Cauchy-Green tensor
$\boldsymbol{D}$	Deformation rate
$\boldsymbol{D}^p$	Plastic strain rate
$\boldsymbol{E}$	Total Green-Lagrange strain tensor
$\boldsymbol{E}^e$	Elastic Lagrangean strain
$\boldsymbol{F}$	Total deformation gradient tensor
$\boldsymbol{E}^*$	Elastic Lagrangian strain
$\boldsymbol{F_e}$	Elastic deformation gradient
$\boldsymbol{F_p}$	plastic deformation gradient
G^e	Elemental incompressibility matrix
g^α	Slip resistance
$h^{\alpha\beta}$	Hardening modulus
$\boldsymbol{I}$	Identity tensor
$\boldsymbol{J}$	Jacobian matrix
K	Global stiffness matrix
$\hat{K}$	Bulk modulus
K^e	Elemental stiffness matrix
$\boldsymbol{L}$	Velocity gradient
$\boldsymbol{L}_p$	Plastic velocity gradient tensor
m	Strain rate sensitivity
$\boldsymbol{M}^\alpha$	Schmid tensor in slip system α
M^e	Elemental pressure mass matrix
$\boldsymbol{m}_\mathbf{0}^\alpha$	Slip direction
n^α	Forest dislocation density

$\boldsymbol{n_0^\alpha}$	Slip plane normal to slip system
N_u'	Velocity shape functions spatial gradients
N_u	Velocity shape function
N_p	Pressure shape function
$\boldsymbol{P}^\alpha$	Symmetric part of the Schmid tensor
$\boldsymbol{Q}^\alpha$	Skew-symmetric part of the Schmid tensor
$\boldsymbol{R}^*$	Symmetric leastic stretch tensor
$\boldsymbol{T}^*$	Second Piola-Kirchhoff stress
$\boldsymbol{V}^*$	Lattice rotation
$\boldsymbol{W}$	Plastic spin
$\boldsymbol{W}^p$	Plastic spin
α	Slip system
τ^α	Resolved shear in slip system α
$\mathbf{\Gamma}$	Matrix of ones with size of 3
$\dot{\gamma}_0$	Reference value of the shearing rate
$\dot{\gamma}^\alpha$	Shearing rate on the slip system α
$\boldsymbol{\epsilon}^*$	Strain
ζ	Fourth order elasticity tensor
κ	Transformation matrix
κ_0	Initial orientation of the crystal
$\boldsymbol{\sigma}$	Cauchy stress
ϑ	Fourth order identity tensor

LIST OF ACRONYMS/ABBREVIATIONS

BCC	Body centered cubic
CP	Crystal Plasticity
CPFEM	Crystal Plasticity Finite Element Method
CPFFT	Crystal Plasticity Fast Fourier Transform
FEM	Finite Element Method
FCC	Face centered cubic
FFT	Fast Fourier Transform
HCP	Hexagonal close packed
ND	Normal Direction
PDE	Partial Differential Equation
RD	Loading Direction
RVE	Representative Volume Element
TD	Transverse Direction

1. INTRODUCTION

The macroscopic properties of most materials are essentially related to their microstructures, and computational microstructure design will play an important part in the development of advanced materials. Most of the research in this area simplifies the problem by working with volume elements significantly larger than a single grain. The study of the relationship between grain structure and material properties involves information at a lower length scale, and still offers many unanswered questions. The fundamental component of modern crystal plasticity is the simulation of the single crystals, and finite element modelling is one of the leading methods.

The crystal plasticity finite element method traditionally involves element volumes much larger than the single crystal volume. This required additional approximations to describe how the deformation of individual crystals was related to the deformation of the elements, as the elements were crystal aggregates. One motivation for these approximations was that it was not possible to resolve the grain structure directly due to the large number of finite elements needed and the limited computational resources. Improvements to those models can be difficult due to the interaction of the crystal plasticity models with the homogenization role though.

The increase in available computational power has given us the opportunity to increase the accuracy of the simulations by more directly simulating behavior on the level of the grains. This is an active field of research, and affords some simplifications like the elimination of the averaging step. It also raises the possibility of other complications, like what happens at the interfaces between two elements with different orientations; grain boundary properties are not well characterized and the mechanisms of slip transference are not well known.

Moreover, constitutive relations can change at smaller length scales. For instance, an aggregate finite element has constitutive relations and hardening laws that are necessarily coarse, since the hardening law can not directly be related to any microscopic

mechanism. As the elements pass below the grain size though, the deformation of the crystal and therefore the deformation of the elements is governed by specific mechanisms like dislocations. We can then have a dislocation-based constitutive model like the one being developed by Raabe and his team [62].

The best way to use the finite element method is at the single crystal level because the deformation of the element can then be connected to more fundamental deformation mechanisms such as dislocation motion. This thesis begins with the method of Kalidindi *et al.* [31], but as this method is based on the homogenization methods, continues with the well-established crystal plasticity finite element framework of Marin and Dawson [46, 47].

Preliminary work has been done to implement the more established model of Cuitino and Ortiz for single crystals as well [14].

2. CRYSTAL PLASTICITY FINITE ELEMENT METHOD

2.1. Historical Review

Crystal plasticity method formulations began with the work of Taylor and Elam [67, 68] in 1923 while they were working on the distortion of aluminum crystal during tensile tests. Taylor then continued his studies in crystal plasticity on plastic deformation and plastic strains in metals [5,6]. The first descriptions of the elastic-plastic behavior of single crystals based on the modern continuum mechanics and constitutive formulations were developed by Hill [26] and Mandel [45]. These constitutive relations were later extended to strain formulations by Rice [60], Hill and Rice [27], Asaro [2,3], and Asaro and Rice [5].

Since the finite element method has the flexibility to handle complex internal and external boundary conditions, it is frequently used in the continuum mechanics area. In 1943, Courant [13] implemented the first finite element simulation and the method was further developed by Zienkiewicz [74], Zienkiewicz *et al.* [75]. Constitutive relations based on an anisotropic yield surface were developed while scientists were trying to interpolate plastic anisotropy using finite element formulations; one of the early relations was proposed by Hill [28] in 1948. His studies were further extended with the works of Barlat and Lian [40], Plunkett *et al.* [57, 58].

The advantage of these methods was their fast calculations, but since the same yield surface was used for each material point and texture evolution was not taken into account, the results generated by this method are not reliable for complex deformation paths. Later models by Van Houtte [70], Li *et al.* [39] and Van Houtte *et al.* [69, 72] included the initial texture of the materials, but could not track the texture evolution which is important in metal forming operations.

Beside the yield surface concept, crystal plasticity applications can be used to study the deformation of materials. In crystal plasticity finite element method, the

behavior of single crystals is modeled using the constitutive equations, and a homogenization method such as the Taylor method [66], relax constraints [33], LAMEL [71], self-consistent [35, 36, 38] is used to predict the evolution of aggregate.

2.2. Crystal Anisotropy

The physical properties of single crystals and polycrystals are directionally dependent, and this causes the material to exhibit elastic and plastic anisotropy in mechanical properties such as Young's modulus, strength, ductility, yield stress and work hardening.

The linear density of atoms is not the same in all crystallographic directions, this is one of the reasons for the anisotropic behavior in single crystals. For polycrystals on the other hand, the crystallographic texture produced during the thermo-mechanical processing history and the evolution of this texture are the major sources of anisotropy. Bearing in mind that the plastic anisotropy of a material has a significant effect on the final shape and dimension of a product, reliable numerical simulation of elasto-plastic deformation and the ability to predict the effect of microstructure on the anisotropy would be significant for material properties optimization and the development of new materials [59].

The distribution of stresses in a polycrystal affects the plastic deformation rate of the composing crystals. Given a change in material state, the stress state needs to be updated to satisfy the compatibility and equilibrium conditions. When the load is not sufficiently high to cause plastic deformation, the deformation is elastic and the elastic modulus controls the stress-strain relationship. When the load increases beyond this threshold, plastic deformation begins and the behavior is governed by the yield surface and deformation gradient [15].

The first function to characterize the anisotropic behavior of metals was based on the isotropic Von Mises yield function, and was developed by Hill in 1948 [28]. This was initially the most popular version of the anisotropic yield surface. Later, numerous

anisotropic yield functions with various levels of accuracy were proposed to increase the anisotropic effects and improve precision in the calculations [1, 7, 8, 41, 42]. The majority of these functions are only useful under plane stress, while the more advanced ones for spatial loading generally use the principal stresses of a linear transformed stress tensor and involve an intricate computation [42].

Utilizing analytical expressions for the yield surface in the finite element method reduces the simulation time which is the primary advantage of this method. The drawback of this approach is the absence of texture evolution during the deformation procedure with the same yield surface at every material point. This leads to significant computational errors when the specimen experiences complicated deformation.

A well-known example of anisotropy during the metal forming process is earing in deep-drawn cans. Figure 2.1 shows the comparison between the earing profiles of a deep-drawn aluminum can using (a) the crystal plascitiy finite element method and (b) experiment. Four ears indicate the anisotropy in the mechanical properties of the aluminum sheet. Classical plasticity, which does not account for crystallographic microstructure, was not able to characterize the metal forming processes illustrated in Figure 2.1.

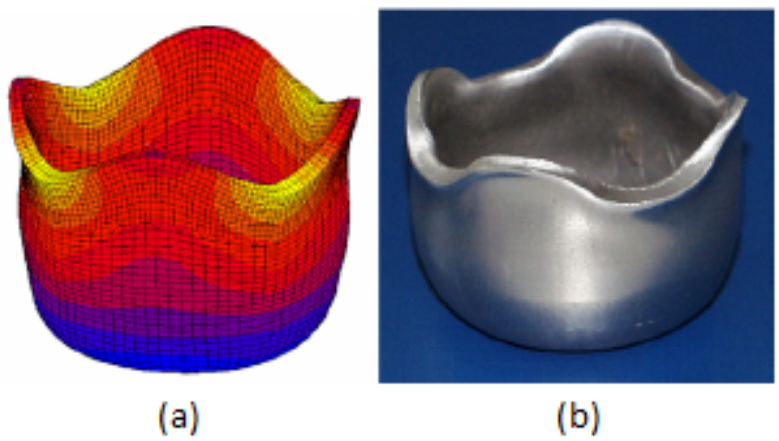


Figure 2.1. Comparison between earing in Aluminum can after cup-drawing: (a) CPFEM simulation (b) experiment [62]

2.3. Crystal plasticity finite element method

Plasticity theories are indispensable for materials modeling, and eventually for the optimization and control of microstructures. Conventional continuum mechanics theories assumed that the stress is a purely local function of other variables like the strain. This is reasonable only when the deformation field is averaged over a length scale much larger than the grain size, meaning that these theories cannot be used for scale-dependent behavior. For instance, they do not capture phenomenon such as the Hall-Petch effect, where decreasing the grain sizes strengthens the material, even though this is of great importance for the evolution of microstructure.

Motivated by these considerations, classical plasticity theories were revised to include an internal length scale by using plastic strain gradients in the classical constitutive equations. When the length scale of the deformation field is large, the strain gradients are small and the conventional plasticity theories are recovered. When the length scale of the deformation field is small compared to the material length scale though, the effect of the strain gradient is seen.

After the failure of the yield surface method to predict material anisotropy, crystal plasticity methodologies began to appear, early on, this method started with the assumption of simple boundary conditions and isotropic models for the materials. The results of these formulations were not reliable though, since it has been known since 1934 [55] that dislocation slip on crystals slip systems during plastic deformation is a major cause of anisotropy. Isotropic material models did not account for these internal interactions inside the polycrystals.

The constitutive relations have since been developed rapidly, and the crystal plasticity constitutive equations are now able to predict single crystal plastic deformations using slip systems and dislocation densities. Homogenization methods were developed to predict the response of polycrystals from single crystal responses, and the crystal plasticity method relates the microscopic and macroscopic properties of a crystalline aggregate [32]. Homogenization methods can be categorized by the local interactions

between grains.

Taylor type (full constraints homogenization) [66] is the simplest and most popular, but can not provide reliable predictions since the polycrystal stress is calculated by volume averaging the stresses of the single crystals. When the simulation is in the single crystal scale, this method does not account for heterogeneities between the grains. Another popular method is the self-consistent model [35,36,38,52] which embeds individual grains in a medium that deforms the average sense of the whole polycrystal. The LAMEL [71] model instead considers the reciprocal influences of neighboring grains by analyzing the stress equilibrium at grain boundaries. The Relaxed constraints [33] model lifts some of the constraints, allows for simplifications in the compatibility conditions.

Various homogenization methods are illustrated in Fig. 2.2.

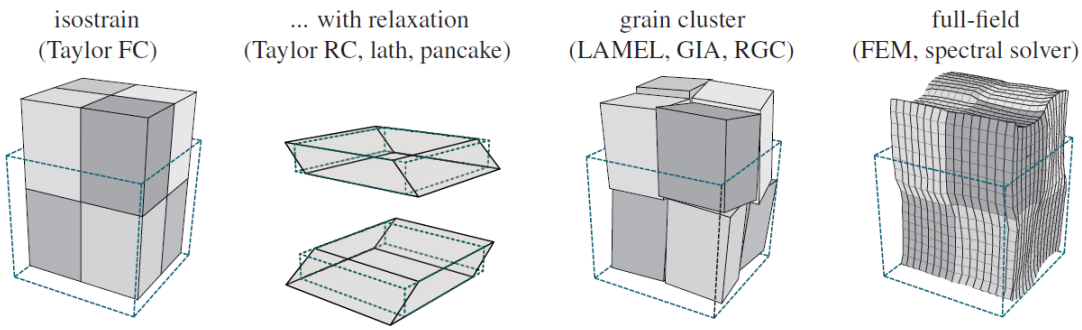


Figure 2.2. Four commonly used homogenization schemes. Reproduced from [61].

The most successful model which takes the local interactions between the grains into account is the crystal plasticity finite element method (CPFEM) [6, 30, 31, 53, 56]. In this method, he response of the aggregate is found using a FE mesh of the microstructure ,with each element considering a single crystallographic orientation. Lattice orientations are updated at each material point using the constitutive relations. The equilibrium and compatibility conditions are solved using a weak form of the

principal of virtual work for each element. The CPFEM is reliable not only for stress-strain relations, but can also be used to analyze the local lattice rotations and the heterogeneity of the single crystals.

One of the main applications of the finite element method in continua is to deal with boundary-value problems. The first CPFEM simulations were performed by Pierce *et al.* in 1982 [55], where two symmetric slip systems were used to examine the tensile response of single crystals. Later studies further developed to two-dimensional polycrystaline simulations using two or three slip systems [24, 25]. The first three dimensional simulations including 12 slip systems were done by Becker in 1991 for FCC single crystals [10] and for columnar polycrystal aggregate in channel die compression [9].

After this breakthrough in CPFEM, numerous methods were developed to enhance the simulation speed and accuracy. At the same time, progressive homogenization methods were appearing and paved the way for the application of CPFEM in large scale simulations [48,63,64,73]. These simulations and studies take dislocation slip into account as the the deformation mechanism and use phenomenological constitutive relations. The CPFEM is significant not only for its ability to account for complicated internal and external boundary conditions, but also for its capability to work with multiple constitutive equations for the calculation of plastic flow and hardening.

The CPFEM is able to take not only stress equilibrium but also strain compatibility into account, and results in a higher accuracy than other methods. This makes CPFEM a reference to test the accuracy of other homogenization methods. The most important parts of the CPFEM are the mesh discretization and microstructure representation. As the complexity of the deformation and boundary conditions increases, a mesh with higher resolution is required to characterize the microstructure and predict the stress and strain responses.

2.3.1. Crystal plasticity models

The CPFEM can incorporate various mechanisms such as dislocation glide (the main source of plastic deformation), mechanical twinning, martensite and shear band formation, or a combination of these mechanisms (Figure 2.3).

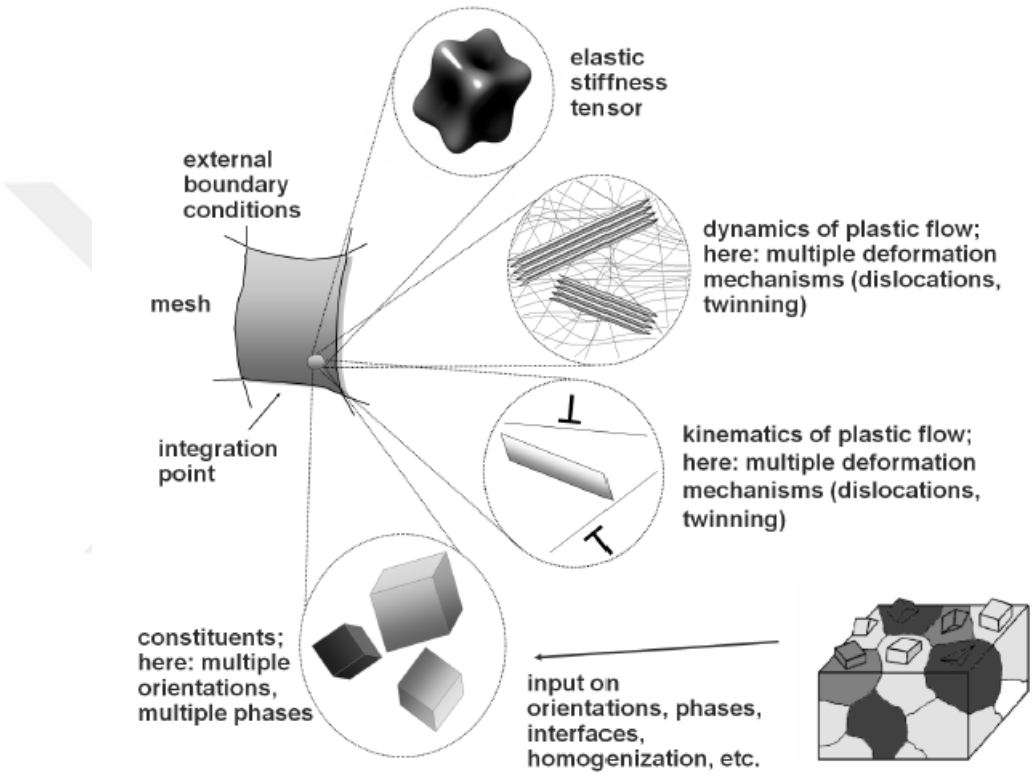


Figure 2.3. Components of CPFEM modelling for a case with multiple deformation mechanisms (dislocation and twinning). [62]

.

The material will deform when it experiences external loads and forces. This deformation may happen in an elastic, plastic or elasto-plastic way. Elastic deformation happens when the external force is not enough to permanently change the atomic arrangement, and hence, is reversible. If the external load is sufficiently strong though, atomic bonds will break and the material deforms plastically. The primary mechanisms for this type of deformation are slip and twinning.

2.3.2. Schmid's law

Schmid's law states that crystallographic slip starts when the shear stress on a slip system exceeds a threshold called the critical resolved shear. For the case of uniaxial tension in Figure 2.4, tensile stress σ is related to resolved shear stress τ by:

$$\tau = \sigma \cos\lambda \cos\phi \tag{2.1}$$

where $\cos\lambda\cos\phi$ is called the Schmid factor.

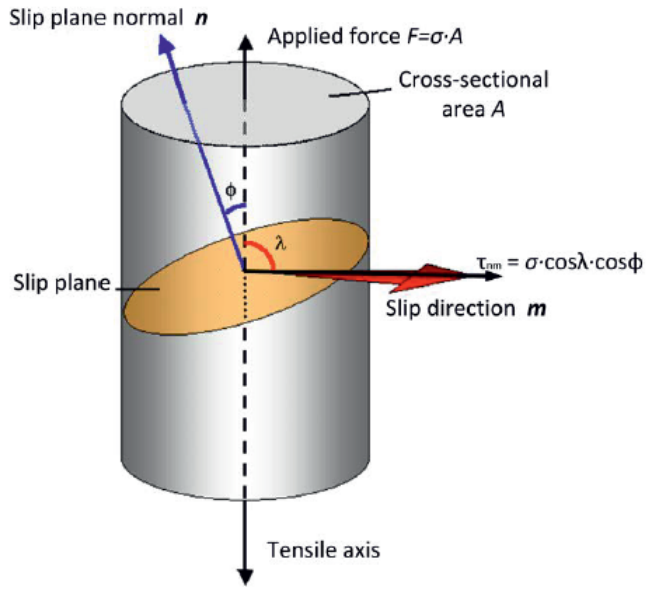


Figure 2.4. Representation of Schmid factor for a sample under uniaxial tension. Reproduced from [16].

The 12 slip systems in FCC metals are listed in Table 2.1, where α is the slip system, $\boldsymbol{m}^{\alpha}$ is slip direction, and $\boldsymbol{n}^{\alpha}$ is the slip plane normal vector. Dislocation slip preferentially occurs in these planes and directions.

The resolved shear stress τ^α for a specific slip system can be formulated as:

$$\tau^\alpha = \boldsymbol{\sigma} : \frac{1}{2}(\boldsymbol{M}^\alpha + \boldsymbol{M}^{\alpha T}) = \boldsymbol{\sigma} : \frac{1}{2}(\boldsymbol{m}^\alpha \otimes \boldsymbol{n}^\alpha + \boldsymbol{n}^\alpha \otimes \boldsymbol{m}^\alpha) \tag{2.2}$$

$$\boldsymbol{M}^\alpha = \boldsymbol{m}^\alpha \otimes \boldsymbol{n}^\alpha \tag{2.3}$$

where $\boldsymbol{\sigma}$ is the Cauchy stress tensor and $\boldsymbol{M}^\alpha$ is the Schmid tensor for slip system α. Since the crystallographic slip does not reorient the texture lattice, the Schmid tensor does not change when the material goes from the reference configuration to the pastically strained intermediate configuration.

Table 2.1. Slip directions $\boldsymbol{m}^\alpha$ and slip plane normals $\boldsymbol{n}^\alpha$ for an FCC crystal.

α	$\boldsymbol{m}^\alpha$	$\boldsymbol{n}^\alpha$	α	$\boldsymbol{m}^\alpha$	$\boldsymbol{n}^\alpha$
1	$\frac{1}{\sqrt{2}}(0,-1,1)$	$\frac{1}{\sqrt{3}}(-1,1,1)$	**7**	$\frac{1}{\sqrt{2}}(0,1,1)$	$\frac{1}{\sqrt{3}}(-1,-1,1)$
2	$\frac{1}{\sqrt{2}}(1,0,1)$	$\frac{1}{\sqrt{3}}(-1,1,1)$	**8**	$\frac{1}{\sqrt{2}}(1,0,1)$	$\frac{1}{\sqrt{3}}(-1,-1,1)$
3	$\frac{1}{\sqrt{2}}(1,1,0)$	$\frac{1}{\sqrt{3}}(-1,1,1)$	**9**	$\frac{1}{\sqrt{2}}(-1,1,0)$	$\frac{1}{\sqrt{3}}(-1,-1,1)$
4	$\frac{1}{\sqrt{2}}(0,-1,1)$	$\frac{1}{\sqrt{3}}(1,1,1)$	**10**	$\frac{1}{\sqrt{2}}(0,1,1)$	$\frac{1}{\sqrt{3}}(1,-1,1)$
5	$\frac{1}{\sqrt{2}}(-1,0,1)$	$\frac{1}{\sqrt{3}}(1,1,1)$	**11**	$\frac{1}{\sqrt{2}}(-1,0,1)$	$\frac{1}{\sqrt{3}}(1,-1,1)$
6	$\frac{1}{\sqrt{2}}(-1,1,0)$	$\frac{1}{\sqrt{3}}(1,1,1)$	**12**	$\frac{1}{\sqrt{2}}(1,1,0)$	$\frac{1}{\sqrt{3}}(1,-1,1)$

2.4. Flow Kinematics and constitutive relations

The followings are the main considerations for the finite element analysis: The first is the finite element mesh which contains the geometric and microstructural information about the region in a piecewise-linear form. The discretization error depends on the reinforcement of the mesh. Second, the boundary conditions and the loading conditions that are applied to the region define the problem to be solved. Third, the problem to be solved the constitutive relations for the material indicate the relation

between the stresses in an element and the strains and deformations of the element. The relationship between the geometric domain and the mesh are illustrated in figure 2.5.

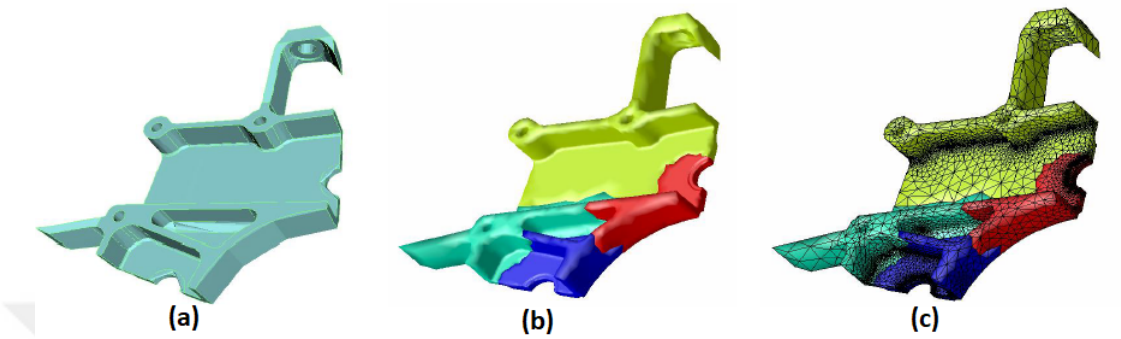


Figure 2.5. Different illustrations of a sample. (a) Geometric model (b) partitioned model (c) partitioned mesh (reproduced from [65]).

Classical phenomenological constitutive laws for crystal plasticity models did not produce reliable predictions [29, 60]. Conventional constitutive relations and models of plasticity do not include size effects, and are not able to explain the behavior of materials on the scale of individual grains. More recent models include early strain gradient plasticity theories like the ones by Mindlin [49,50] which contained high order continuum theories. Later approaches used higher order equilibrium equations and additional boundary conditions to modify conventional continuum theories. These were primarily done by Fleck and Hutchinson [17–19] and Gao *et al.* [21,22]. Strain gradient theories were developed when high accuracy models were needed [37, 51]. Dislocation densities were incorporated into constitutive laws with the works of Gao and Huang [23] and Ma *et al.* [44].

When the crystal is under an applied force, it deforms with kinematics that rely on a multiplicative division of the total deformation gradient tensor $\boldsymbol{F}$ into elastic $\boldsymbol{F}_e$ and plastic $\boldsymbol{F}_p$ components [4]:

$$\boldsymbol{F} = \boldsymbol{F}_e \boldsymbol{F}_p \tag{2.4}$$

$\boldsymbol{F}_e$ represents the deformation gradient caused by elastic stretching, and $\boldsymbol{F}_p$ defines the deformation gradient caused by plastic deformation. The plastic deformation $\boldsymbol{F}_p$ is a permanent deformation associated with the plastic shearing which happens on a slip system α with a vector normal to the slip plane $\boldsymbol{n}^\alpha$ and the corresponding slip direction $\boldsymbol{m}^\alpha$. This deformation stays even after the external forces is removed, and application of $\boldsymbol{F}_p$ alone brings the material into a new configuration called the intermediate or relaxed configuration in Figure 2.6. This configuration is an imaginary state which is free from internal and external forces, but helps us to understand and formulate inelastic deformation in continuum mechanics.

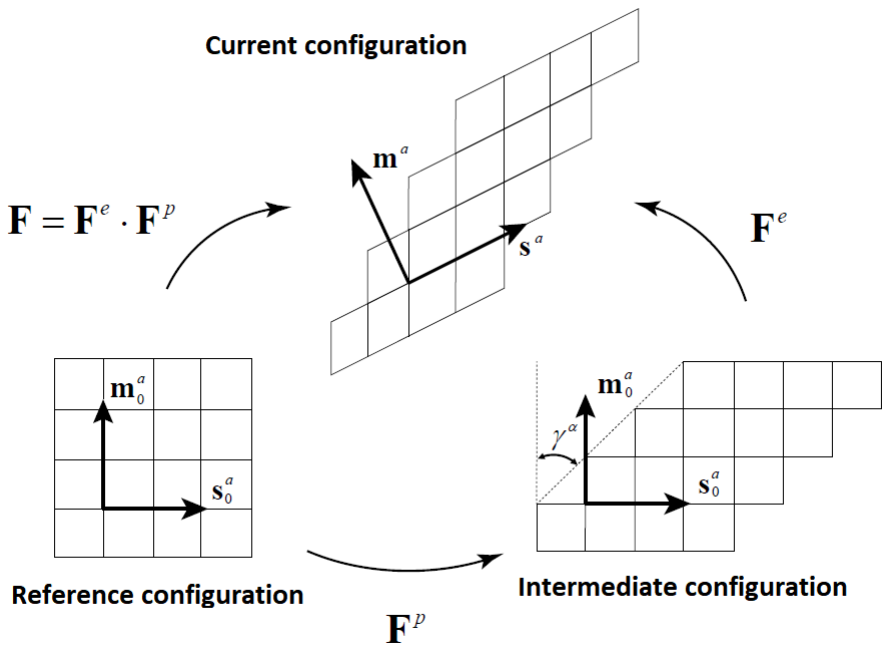


Figure 2.6. Deformation gradient multiplicative decomposition into elastic and plastic parts. Reproduced from [43].

The elastic deformation, on the other hand, is a reversible reaction of the material to the applied forces. The elastic deformation tensor $\boldsymbol{F}_e$ describes this rigid-body rotation and elastic stretching, can be further decomposed into the lattice rotation $\boldsymbol{R}^*$ and the symmetric elastic stretch tensor $\boldsymbol{V}^*$. Hence, the deformation gradient can be written as [47].

$$\boldsymbol{F} = \boldsymbol{R}^* \boldsymbol{V}^* \boldsymbol{F}_p \tag{2.5}$$

The crystal constitutive equations could be expressed in the intermediate (relaxed) configuration or in the current configuration. In this thesis the equations are written in the intermediate configuration.

The velocity gradient can be formulated as:

$$\boldsymbol{L} = \dot{\boldsymbol{F}} \cdot \boldsymbol{F}^{-1} = \dot{\boldsymbol{V}}^* \cdot \boldsymbol{V}^{-1} + \boldsymbol{V}^* \cdot \dot{\boldsymbol{R}}^* \cdot \boldsymbol{R}^{*T} \cdot \boldsymbol{V}^{*-1} + \boldsymbol{V}^* \cdot \boldsymbol{R}^* \cdot \dot{\boldsymbol{F}}_p \cdot \boldsymbol{F}_{p-1} \cdot \boldsymbol{R}^{*T} \cdot \boldsymbol{V}^{*-1} \tag{2.6}$$

The plastic velocity gradient $\boldsymbol{L}_p$ which results from the dislocation slip can be expressed as:

$$\boldsymbol{L}_p = \dot{\boldsymbol{F}}_p \boldsymbol{F}_p^{-1} = \sum_a^n \dot{\gamma}^\alpha \boldsymbol{m}^\alpha \otimes \boldsymbol{n}^\alpha \tag{2.7}$$

where $\dot{\gamma}^\alpha$ is the shearing rate in slip system α due to dislocation slip. In rate dependent formulations [4, 29, 54], the shearing rate on every slip system is related to the resolved shear stress τ^α and slip resistance g^α [31]:

$$\dot{\gamma}^\alpha = \dot{\gamma}_0 \left| \frac{\tau^\alpha}{g^\alpha} \right|^{\frac{1}{m}} \operatorname{sgn}(\tau^\alpha) \tag{2.8}$$

Here $\dot{\gamma}_0$ is the reference value of the shearing rate, m is the strain rate sensitivity, and τ^α is:

$$\tau^\alpha \approx \boldsymbol{T}^* : \boldsymbol{m}_0^\alpha \otimes \boldsymbol{n}_0^\alpha \tag{2.9}$$

The classical constitutive equation can be written as:

$$\boldsymbol{T}^* = \zeta \boldsymbol{E}^* \tag{2.10}$$

Here ζ is the fourth order elasticity tensor and $\boldsymbol{T}^*$ and $\boldsymbol{E}^*$ are the Second Piola-Kirchhoff stress and the elastic Lagrangian strain measures respectively. These are defined from the elastic deformation gradient tensor:

$$\boldsymbol{T}^* = \boldsymbol{F}_e^{-1}[(det\boldsymbol{F}_e)\boldsymbol{\sigma}]\boldsymbol{F}_e^{-T} \tag{2.11}$$

$$\boldsymbol{E}^* = \frac{1}{2}(\boldsymbol{F}_e^T\boldsymbol{F}_e - \boldsymbol{I}) \tag{2.12}$$

Here $\boldsymbol{\sigma}$ is the Cauchy Stress in the crystal and $\boldsymbol{I}$ is the identity tensor.

2.5. Crystal plasticity Fast Fourier Transform Method

The Fast Fourier Transformation (FFT) method is a spectral method in Fourier space that is an alternative to the finite element method for solving partial differential equations (PDE). This includes crystal plasticity formulations.

As seen in Figure 2.7, the deformed configuration for the representative volume element after 40% of thickness reduction is illustrated for the finite element and fast Fourier transform methods. Here, RD is the loading direction, TD is the transverse direction and ND is the normal direction. The distributions of accumulated plastic strain

and stress for the finite element and fast Fourier transform methods applied to a rolling simulation are shown in Figure 2.8, where the figures are plotted on the undeformed structure of the representative volume element. Notice that the stress distribution for both models match.

Both finite element and FFT methods are full-field approaches and perform well in nonlinear cases. They give similar results if there are not large grain distortions in the polycrystal as seen in Figures 2.7 and 2.8. The FFT model is faster since the computation time for similar levels of discretization can be a few seconds for the FFT, while the finite element method needs about a minute [12]. The finite element method also introduces the complication of explicity following the mesh geometry. 3D meshing of microstructures in the finite element method is time consuming and difficult, and makes the calculations complicated when combined with a large number of degrees of freedom. The fast Fourier transform method does not need a mesh [59], but the microstructure is required to be periodic. This is the reason that finite element method is preferred for this thesis, namely, the continuously changing boundary conditions of finite strain crystal plasticity cannot be handled by the FFT method.

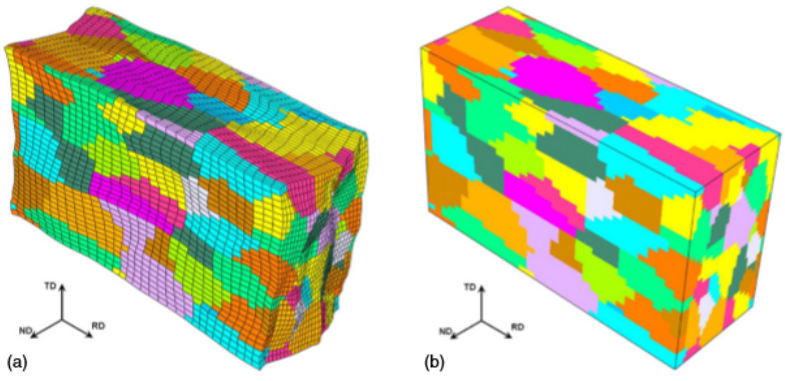


Figure 2.7. Deformed configuration of the RVE from simulations after 40% thickness reduction. (a) FE (b) FFT. Reproduced from [59].

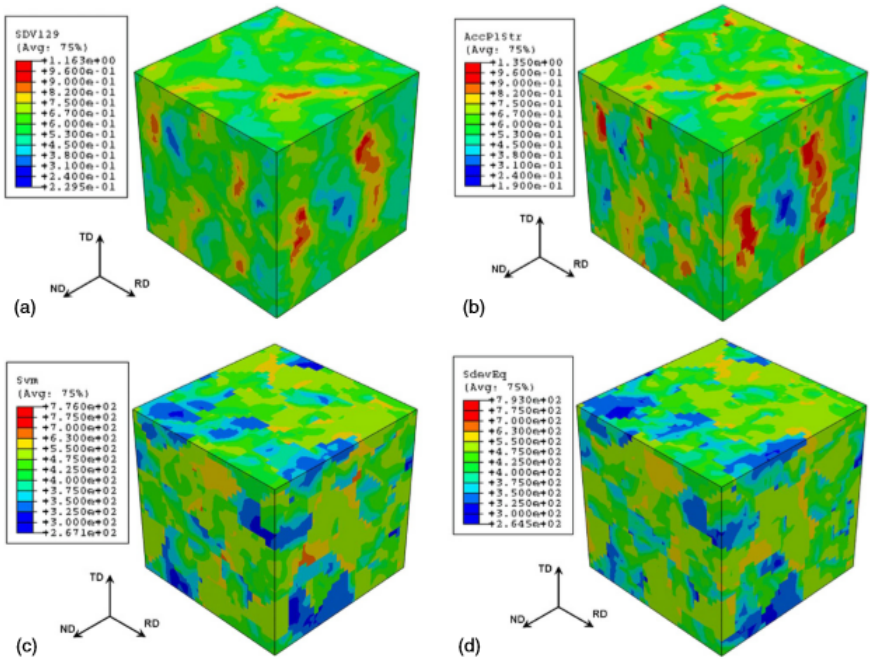


Figure 2.8. Results from rolling simulations. Top row: distribution of accumulated plastic strain. Bottom row: stress distribution. Left: FE. Right: FFT. Reproduced from [59].

3. PROCEDURE AND RESULTS

Small scale and large scale applications can be analyzed with crystal plasticity finite element modeling. Small scale simulations are those for which the size of an element in the finite element mesh is smaller than or equal to the grain size, whereas large scale simulations have more than one crystal at each integration point.

Our procedure began with an implementation of a 2D elasticity problem [11] using the finite element method in MATLAB. This implementation involved three parts:

(i) Pre-processing included constants and material properties, structural definitions, and finite element discretization.

(ii) Processing where elements were initialized, boundary conditions were applied, and the stress and strain fields were found.

(iii) Post-processing where the results from the former section were being presented.

The implementation of the 2D problem was extended to a 3D elasticity problem. This involved modifying the generation of nodes, elements, meshing, Gaussian quadrature and Lagrangian basis. After the definition of the nodes the elements were constructed, and the nodes and elements formed the finite element mesh. A simple mesh is illustrated in Figure 3.1, with 4 node tetrahedral elements with 3-node triangular face elements.

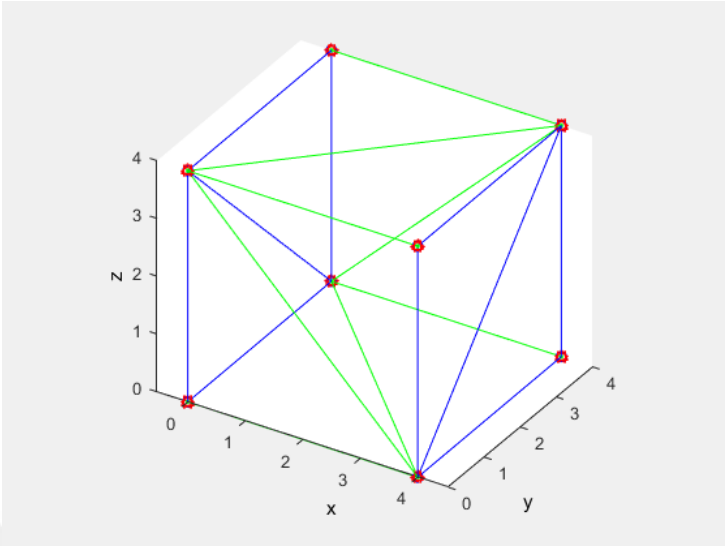


Figure 3.1. Illustration of a finite element mesh where four-node tetrahedral elements compose a cube.

3.1. Viscoelasto-plastic deformation model (Kalidindi's method and results)

The elastic models prior to this point built familiarity with finite elements, but needed plasticity to more accurately reproduce material behavior. One of the earliest elasto-plastic models was the work of Kalidindi, Bronkhorst and Anand [31], where an implicit model for the polycrystaline constitutive relations was presented and implemented in a finite element script. These calculations can be performed using a predictor-corrector method as shown in Figure 3.2. This figure contains a clockwise loop of calculations, where $\boldsymbol{T}^*$ is the second Piola-Kirchhoff stress, $\dot{\gamma}^\alpha$ is the shearing rate on the slip system α, $\boldsymbol{L}_p$ is the plastic velocity gradient, $\boldsymbol{m}^\alpha$ and $\boldsymbol{n}^\alpha$ are the slip direction and slip plane normal to the slip system α, $\boldsymbol{F}_p$ and $\boldsymbol{F}_e$ are the plastic and elastic deformation gradients, $\boldsymbol{C}$ is the elasticity tensor, and $\boldsymbol{I}$ is the identity tensor.

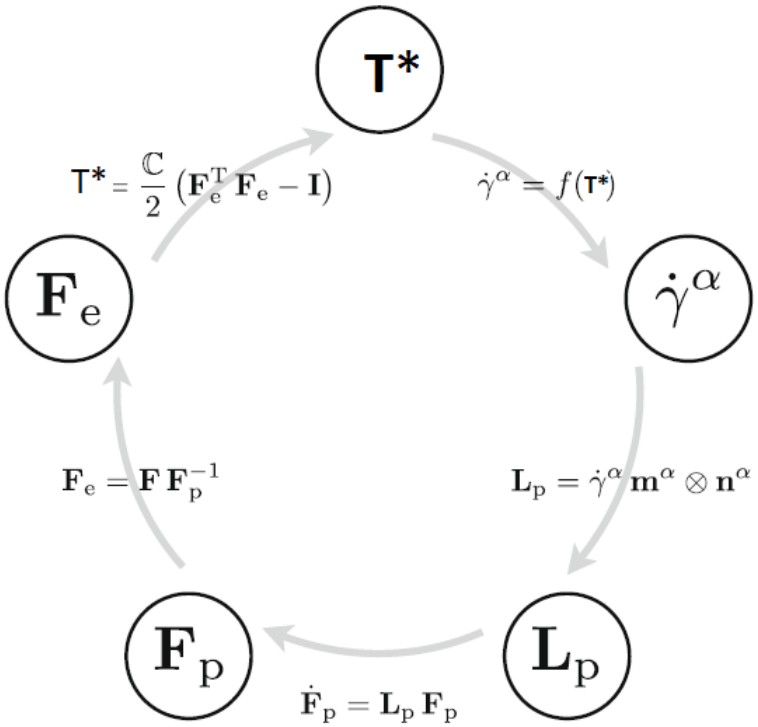


Figure 3.2. Calculation scheme to determine $\boldsymbol{T}^*$ as a function of $\boldsymbol{F}$ [49].

The prediction can start with the shear rates $\dot{\gamma}^\alpha$, the second Piola-Kirchhoff stress $\boldsymbol{T}^*$, or the elastic or plastic deformation gradient $\boldsymbol{F}_e$ and $\boldsymbol{F}_p$. Once the coefficient to begin with is initialized, the prediction can continue using a Newton-Raphson scheme [31].

In the fully implicit time integration method of Kalidindi, quantities which are supposed to be known at the beginning of the simulation are:

(i) Initial time-independent slip planes and slip directions ($\boldsymbol{m}_0{}^\alpha$,$\boldsymbol{n}_0{}^\alpha$)

(ii) Total deformation gradient at time step t ($\boldsymbol{F}_{(t)}$), and an approximation of deformation gradient for the next time step ($\boldsymbol{F}_{(\tau)}$)

(iii) Plastic deformation gradient at time step t ($\boldsymbol{F}^{p}{}_{(t)}$)

(iv) Initial value of slip resistance (g_0)

A two level iterative scheme is used for the modelling, with the first level an iteration over the second Piola-Kirchhoff stress. After the convergence of the first level, the second level iterates over slip resistances ($g^{\alpha}{}_{(\tau)}$). The calculations start with an initial guess for the second Piola-Kirchhoff stress $\boldsymbol{T}^{*}$. This guess is used for the calculation of resolved shear stresses τ^{α}:

$$\tau^{\alpha} \approx \boldsymbol{T}^{*} : \boldsymbol{m}_0^{\alpha} \otimes \boldsymbol{n}_0^{\alpha} \tag{3.1}$$

The first level of iterations continues until the convergence of the stress, and then the values of other coefficients are updated based on the converged stress value. The initial trial value for the second Piola-Kirchhoff stress is:

$$\boldsymbol{T}^{*tr} = \zeta[(1/2)\{\boldsymbol{A} - \boldsymbol{I}\}] \tag{3.2}$$

where ζ is the fourth order elasticity tensor and $\boldsymbol{A}$ is calculated from:

$$\boldsymbol{A} = \boldsymbol{F}_{(t)}^{p-T} \boldsymbol{F}_{(\tau)}^{T} \boldsymbol{F}_{(\tau)} \boldsymbol{F}_{(t)}^{p-1} \tag{3.3}$$

The Second Piola-Kirchhoff stress for the next time step can be obtained from:

$$\boldsymbol{T}^{*}{}_{(\tau)} = \boldsymbol{T}^{*tr} - \sum_{\alpha} \Delta\gamma^{\alpha} \boldsymbol{C}^{\alpha} \tag{3.4}$$

where $\boldsymbol{C}^{\alpha}$ is equal to:

$$\boldsymbol{C}^{\alpha} = \zeta[(1/2)\boldsymbol{B}^{\alpha}] \tag{3.5}$$

and

$$\boldsymbol{B}^{\alpha} = \boldsymbol{A}\boldsymbol{S_0}^{\alpha} + \boldsymbol{S_0}^{\alpha T}\boldsymbol{A} \tag{3.6}$$

After calculation of $\boldsymbol{T}^*$, a Newton-Raphson scheme is used to converge the second Piola-Kirchhoff stress:

$$\boldsymbol{T}^*{}_{n+1}(\tau) = \boldsymbol{T}^*{}_n(\tau) - \Upsilon_n^{-1}[\boldsymbol{G}_n] \tag{3.7}$$

where $\boldsymbol{G_n}$ and Υ_n are calculated as:

$$\boldsymbol{G_n} = \boldsymbol{T}^*{}_n(\tau) - \boldsymbol{T}^{*tr} + \sum_{\alpha} \Delta\gamma^{\alpha}\boldsymbol{C}^{\alpha} \tag{3.8}$$

$$\Upsilon_n = \vartheta + \sum_{\alpha} \boldsymbol{C}^{\alpha} \otimes \frac{\partial}{\partial \boldsymbol{T}^*{}_n(\tau)} \Delta\gamma^{\alpha} \tag{3.9}$$

In the recent equations n indicates the iteration number and ϑ is the fourth order identity tensor. The convergence of $\boldsymbol{T}^*$ is defined based on the criterion:

$$\Delta\boldsymbol{T}^* = \boldsymbol{T}^*{}_{n+1}(\tau) - \boldsymbol{T}^*{}_n(\tau) \tag{3.10}$$

If the value of $|\Delta\boldsymbol{T}^*|$ is less than a limit ηs_0, the stress is converged. If the convergence condition is not satisfied when the maximum number of iterations is reached, the value of $\boldsymbol{T}^*$ is updated using the equation:

$$\boldsymbol{T}^*{}_{n+1}(\tau) = \boldsymbol{T}^*{}_n(\tau) + \eta s_0 \ \mathrm{sgn}\{\Delta\boldsymbol{T}^*\} \tag{3.11}$$

where g_0 is the initial slip system resistance and the constant η is taken as $\frac{2}{3}$. After the convergence of $\boldsymbol{T}^*$, the second level of iterations starts with the aim of converging g^α:

$$g^\alpha_{k+1} = g^\alpha(t) + \sum_\beta h^{\alpha\beta}(g^\beta(\tau)) \left|\Delta\gamma^\beta\right| \tag{3.12}$$

Here, the term $h^{\alpha\beta}$ indicates the hardening modulus which consists of the slip hardening rate $h^{(\beta)}$ and the matrix $q^{\alpha\beta}$ which describes the latent hardening behavior of the aggregate.

$$h^{\alpha\beta} = q^{\alpha\beta} h^{(\beta)} \tag{3.13}$$

$$q^{\alpha\beta} = \begin{bmatrix} \mathbf{\Gamma} & q\mathbf{\Gamma} & q\mathbf{\Gamma} & q\mathbf{\Gamma} \\ q\mathbf{\Gamma} & \mathbf{\Gamma} & q\mathbf{\Gamma} & q\mathbf{\Gamma} \\ q\mathbf{\Gamma} & q\mathbf{\Gamma} & \mathbf{\Gamma} & q\mathbf{\Gamma} \\ q\mathbf{\Gamma} & q\mathbf{\Gamma} & q\mathbf{\Gamma} & \mathbf{\Gamma} \end{bmatrix} \tag{3.14}$$

$\mathbf{\Gamma}$ is a matrix of ones with size of 3. and q is the ratio of the latent hardening rate to self hardening rate.

When both levels of iterations converge, the updated values for elastic and plastic deformation gradients can be calculated. The updated $h^{(\beta)}$ is obtained from:

$$h^{(\beta)} = h_0\{1 - \frac{g^\beta}{g_s}\}^a \tag{3.15}$$

where h_0, a and g_s are hardening parameters which are taken to be identical for all slip systems.

The material properties for the annealed OFHC copper which is used in this simulation are described in Table 3.1.

Table 3.1. material parameters for annealed OFHC copper

Elastic shear	$\hat{K}$	m	γ_0	h_0	s_s	s_0	q
46.5 GPa	124 GPa	0.012	0.001 sˆ-1	180 MPa	27.17 GPa	16 MPa	1.4

Implementing this time-integration procedure in MATLAB and plotting Von-Mises stress vs time produces the following result:

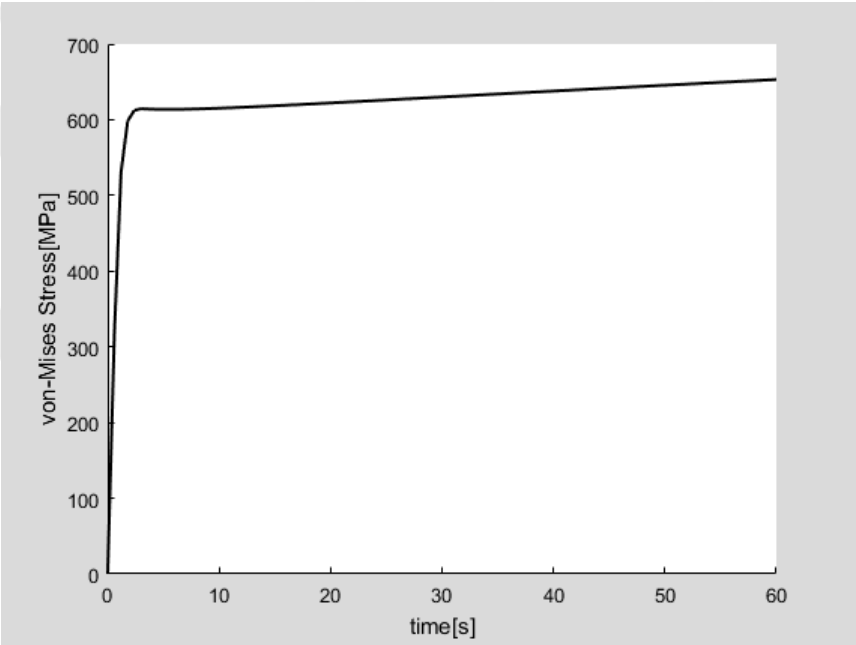


Figure 3.3. Von-Mises - time plot of Kalidindi's time-integration procedure.

3.2. Viscoelasto-plastic deformation model (Marin and Dawson's method and results)

Since Kalidindi's method focuses on homogenization structures for application in polycrystalline simulations, we then worked on Marin and Dawson's method because we were able to find references where they actually applied this to the single crystal scale [46, 47]. The constitutive equations for Marin and Dawson's model start with

the decomposition of the deformation gradient into elastic and plastic parts, as seen in Figure 3.4.

$$\boldsymbol{F} = \boldsymbol{V}^* \boldsymbol{R}^* \boldsymbol{F}^p \tag{3.16}$$

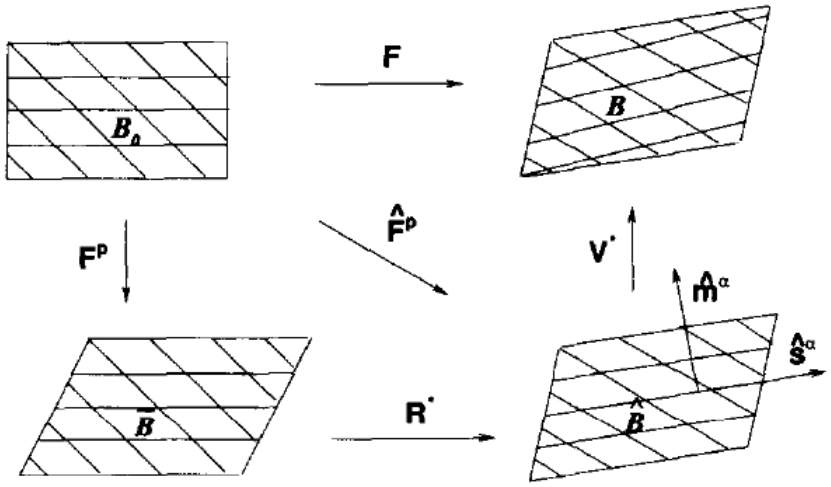


Figure 3.4. Decomposition of deformation gradient into elastic and plastic parts [46].

where $\boldsymbol{F}^p$, $\boldsymbol{V}^*$ and $\boldsymbol{R}^*$ are the purely plastic deformation gradient, the symmetric left elastic stretch tensor, and lattice rotation, respectively.

The procedure begins with an initial guess for the velocity vector $\{U\}_g$ and calculation of updated coordinates $\{x\}_g$ at time step $t + \Delta t$ using this this velocity vector:

$$\{x\}_g = \{x\}_t + \Delta t \{U\}_g \tag{3.17}$$

The velocity gradient can be obtained using the spatial rate change in the velocity:

$$\boldsymbol{L} = \frac{\Delta v}{\Delta x} \tag{3.18}$$

This velocity gradient can be decomposed into symmetric and skew-symmetric parts, where the symmetric part is the deformation rate $\boldsymbol{D}$ which indicates the instantaneous rate of stretching of the material, and the skew-symmetric part $\boldsymbol{W}$ indicates the plastic spin and the rate of rigid-body rotation in the material:

$$\boldsymbol{L} = \boldsymbol{D} + \boldsymbol{W} \tag{3.19}$$

The volumetric part of the deformation rate can be used to calculate the volumetric part of the strain for the next time step $\boldsymbol{\epsilon}^*_{kk}$ using the backward Euler method:

$$\boldsymbol{\epsilon}^*_{kk} = \bar{\boldsymbol{\epsilon}}^*_{kk} + \Delta t \boldsymbol{D}_{kk} \tag{3.20}$$

The volumetric part of the Kirchhoff stress can be obtained using the volumetric part of the strain and the Lame constants:

$$\boldsymbol{\tau}_{kk} = (2\mu + 3\lambda)\boldsymbol{\epsilon}^*_{kk} \tag{3.21}$$

After calculation of the elemental velocity gradient, the time integration of the crystal constitutive calculations begins [47]. The process is followed in the lattice fixed reference frame and the orientation of the crystal is defined using the transformation matrix κ. This matrix is defined as:

$$\kappa = \kappa_0 \boldsymbol{R}^* \tag{3.22}$$

where $\boldsymbol{R}^*$ is the rotation tensor and κ_0 is the initial orientation of the crystal.

The iterative procedure of Marin and Dawson [47], uses three levels of iteration. The first level converges the Kirchhoff stress using fixed values of the rotation $\boldsymbol{R}^*$ and the hardness g^α, which are generated using the estimated values of the deviatoric

Kirchhoff stress $\boldsymbol{\tau}'$:

$$\left(\sum_{\alpha=1}^{n}\frac{\partial\dot{\gamma}^{\alpha}}{\partial\tau^{\alpha}}\right)\{\boldsymbol{P}^{\alpha}\}\{\boldsymbol{P}^{\alpha}\}^{T}=\{\boldsymbol{D'}\}\{\boldsymbol{D}^{p}\} \tag{3.23}$$

$$g^{\alpha}=\bar{g}^{\alpha}+\Delta t\dot{g}^{\alpha} \tag{3.24}$$

Here, $\bar{g}^{\alpha}$ is the hardness in the current time step. The value of $\boldsymbol{R}^{*}$ for the next time step can be calculated by the exponential map:

$$\boldsymbol{R}^{*}=\exp(\bar{\boldsymbol{\Omega}})\bar{\boldsymbol{R}}^{*} \tag{3.25}$$

where $\bar{\boldsymbol{R}}^{*}$ is the rotation in the current time step and $\bar{\boldsymbol{\Omega}}$ is calculated from:

$$\bar{\boldsymbol{\Omega}}=(\boldsymbol{W}-\sum_{\alpha}\dot{\gamma}^{\alpha}\boldsymbol{Q}^{\alpha})\Delta t \tag{3.26}$$

Here, g^{α} and $\boldsymbol{R}^{*}$ are the initial estimates for the first level of iteration, and $\boldsymbol{Q}^{\alpha}$ indicates the skew-symmetric part of the Schmid tensor. The first level of the convergence scheme for the deviatoric part of the Kirchhoff stress is begun by fixing g^{α} and $\boldsymbol{R}^{*}$ at their respective best guesses:

$$[\bar{\boldsymbol{A}}]\{\Delta\boldsymbol{\tau}\}'=-2\mu\Delta t\{\boldsymbol{B}\} \tag{3.27}$$

$\boldsymbol{B}$ is a residual and $\bar{\boldsymbol{A}}$ is the fourth order Jacobian tensor, these are defined elsewhere [47]. The iterations continue until the change in the values of the $\boldsymbol{\tau}'$ falls below $10^{-4}g_0$.

After the convergence of the stress, the second level of iterations begins to converge the hardness and rotation parameters. Equation 3.28 is used to calculate the updated Δg:

$$\left(1-\Delta t\frac{\partial\dot{g}^{\alpha}}{\partial g^{\alpha}}\right)\Delta g^{\alpha}=-g^{\alpha}+\bar{g}^{\alpha}+\Delta t\dot{g} \tag{3.28}$$

When this value falls below $10^{-3}g_0$ $\boldsymbol{R}^*$ is also taken to be converged. After all coefficients in the previous two levels of iteration have converged, the third level of iterations begins by calculating the deviatoric deformation rate:

$$\{\boldsymbol{D}'\} = \frac{1}{\Delta t}\{\boldsymbol{\epsilon}^{*'}\} + \{\boldsymbol{D}^p\} + [\boldsymbol{W}^p]\{\boldsymbol{\epsilon}^{*'}\} - \frac{1}{\Delta t}\{\bar{\boldsymbol{\epsilon}}^{*'}\} \tag{3.29}$$

where $\{\boldsymbol{\epsilon}^{*'}\}$ is defined as:

$$\{\boldsymbol{\epsilon}^{*'}\} = \frac{1}{2\mu}\{\boldsymbol{\tau}'\} \tag{3.30}$$

where,

$$\{\boldsymbol{\tau}'\} = \beta\{\boldsymbol{\sigma}'\} \tag{3.31}$$

and

$$\beta = \det(\boldsymbol{I} + \boldsymbol{\epsilon}^*) \tag{3.32}$$

$\{\boldsymbol{D}^p\}$ is defined as:

$$\{\boldsymbol{D}^p\} = [\boldsymbol{\Phi}]\{\boldsymbol{\tau}'\} \tag{3.33}$$

where

$$[\boldsymbol{\Phi}] = \sum_{\alpha=1}^{n} \frac{\dot{\gamma}^\alpha}{\tau^\alpha}\{\boldsymbol{P}^\alpha\}\{\boldsymbol{P}^\alpha\}^T \tag{3.34}$$

and $\boldsymbol{P}^\alpha$ is the symmetric part of the Schmid tensor.

The deviatoric stress of the crystal can be obtained using:

$$\{\boldsymbol{\sigma}'\} = [\boldsymbol{S}]\{\boldsymbol{D}'\} - \{H\} \tag{3.35}$$

where $[S]$ and $\{\mathrm{H}\}$ are the macroscopic stiffness matrix and macroscopic vector which can be written as:

$$[S] = \langle [\tilde{\boldsymbol{C}}]^{-1} \rangle \tag{3.36}$$

$$\{H\} = \langle [\tilde{\boldsymbol{C}}]^{-1} \{h\} \rangle \tag{3.37}$$

where

$$h = [\boldsymbol{W}^p]\{\boldsymbol{\epsilon}'\} - \frac{1}{\Delta t}\{\bar{\boldsymbol{\epsilon}}^{*'}\} \tag{3.38}$$

The symmetric crystal compliance matrix is given by

$$[\tilde{\boldsymbol{C}}] = \frac{\beta}{2\mu\Delta t}[\boldsymbol{I}] + \beta[\boldsymbol{\Phi}] \tag{3.39}$$

Using the standard finite element procedure, the equation to be solved to find the velocity and pressure field is represented below,

$$\begin{bmatrix} K & G \\ G^T & -M \end{bmatrix} \begin{Bmatrix} U \\ -P \end{Bmatrix} = \begin{Bmatrix} f \\ -g \end{Bmatrix} \tag{3.40}$$

This can be separated into separate equations for the nodal velocities U and the pressures P:

$$([K] + [G][M]^{-1}[G]^T)\{U\} = \{f\} - [G][M]^{-1}\{g\} \tag{3.41}$$

The coefficients in this global system are described below, $[K^e]$ is the elemental stiffness matrix:

$$[K^e] = \int [N_u']^T [X]^T [S][X][N_u'] dV \tag{3.42}$$

$[N_u']^T$ is a $6 \times 3n_u$ matrix of spatial gradients for the velocity shape functions, $[S]$ is the macroscopic stiffness matrix, and $[X]$ is the matrix which converts a 6×1 vector into a 5×1 matrix as shown below:

$$[X] = \begin{bmatrix} \frac{1}{\sqrt{2}} & -\frac{1}{\sqrt{2}} & 0 & 0 & 0 & 0 \\ -\frac{1}{\sqrt{6}} & -\frac{1}{\sqrt{6}} & \frac{\sqrt{2}}{\sqrt{3}} & 0 & 0 & 0 \\ 0 & 0 & 0 & \sqrt{2} & 0 & 0 \\ 0 & 0 & 0 & 0 & \sqrt{2} & 0 \\ 0 & 0 & 0 & 0 & 0 & \sqrt{2} \end{bmatrix} \tag{3.43}$$

$[G^e]$ is the elemental incompressibility matrix:

$$[G^e] = \int [N_u']^T \{\delta\} \{N_p\}^T dV \tag{3.44}$$

$\{N_p\}$ is the $n_p \times 1$ vector of pressure shape functions, n_p is the nodal points for the pressure, and $\{\delta\}$ is the trace operator vector as described below:

$$\{\delta\} = \begin{Bmatrix} 1 & 1 & 1 & 0 & 0 & 0 \end{Bmatrix} \tag{3.45}$$

$[M^e]$ is the elemental pressure mass matrix:

$$[M^e] = \int \frac{\beta}{\Delta t \hat{K}} \{N_p\} \{N_p\}^T dV \tag{3.46}$$

where $\hat{K}$ is the bulk modulus which can be calculated using Lame's constants as: $\hat{K} = \frac{2}{3}\mu + \lambda$.

Finally, $\{b\}$ and $\{t\}$ are the vectors of body forces and tractions:

$$\{f^e\} = \int [N_u']^T [X]^T \{H\} dV + \int [N_u]^T \{b\} dV + \int [N_u]^T \{t\} dA \tag{3.47}$$

where $[N_u]$ is the $3 \times 3n_u$ matrix of velocity shape functions and n_u shows the velocity nodal points, and

$$\{g^e\} = \int \frac{1}{\Delta t}\{N_p\}\mathrm{tr}(\bar{\epsilon}^*)dV \tag{3.48}$$

After the calculation of the elemental operators for these coefficients, they need to be scattered into the global system operators, After the convergence of the velocity field, the pressure field {P} can be calculated using

$$\{P\} = -[M]^{-1}(\{g\} + [G]^T\{U\}) \tag{3.49}$$

and the third level iteration is completed. At the end of each time step, the converged values of coefficients are set as the best guesses for the beginning of the next time step.

3.2.1. Investigating the Effect of Number of Elements in Stress Relaxation Tests

For the single crystal simulations, convergence was studied as a function of the number of elements and the length of time step. Afterwards, the effect of the crystal direction along which force was applied was considered. Two loading cases of stress relaxation and reverse loading were examined for the single crystal and polycrystal models.

For the stress relaxation experiment, the sample is under compression until the effective strain reaches a threshold value of $\epsilon = 0.5$, at which point the load is released and the relaxation process starts. The initial crystal orientation is defined randomly unless otherwise specified, and the material properties of the Al-1100 which is used in the simulation are defined in Table 3.1.

Table 3.2. material parameters

μ	λ	m	$\dot{\gamma_0}$	h_0	g_0	g_{s0}	m'	$\dot{\gamma_{s0}}$
25.3 GPa	54.4 GPa	0.05	$1.0s^{-1}$	58.41 GPa	27.17 GPa	61.80 MPa	0.005	$5.0 \times 10^{10}s^{-1}$

The elastic stiffness matrix is defined using Lame's constants in Table 3.1 as:

$$\zeta = \begin{bmatrix} 2\mu+\lambda & \lambda & \lambda & 0 & 0 & 0 \\ \lambda & 2\mu+\lambda & \lambda & 0 & 0 & 0 \\ \lambda & \lambda & 2\mu+\lambda & 0 & 0 & 0 \\ 0 & 0 & 0 & \mu & 0 & 0 \\ 0 & 0 & 0 & 0 & \mu & 0 \\ 0 & 0 & 0 & 0 & 0 & \mu \end{bmatrix} \tag{3.50}$$

The initial meshing of the sample is shown in Figure 3.6. In this example, there is one element along each each axis, the sample is under compression in the $-z$ direction along the $\langle 100 \rangle$ crystal direction and the simulation lasts 150 time steps. The boundary conditions for the relaxation case fix the 1st node (bottom left front) in the x, y and z directions, the node which is corresponding to the $(nnx + 1)$ where nnx is number of nodes in x direction (bottom right front), in y and z directions, and all the bottom nodes in the z direction. The top face nodes are displaced with a constant velocity (strain control). As illustrated in Figure 3.6, the cubic sample being analyzed consists of four-noded tetrahedral elements (Figure 3.5), with a total of 8 nodes and 5 elements.

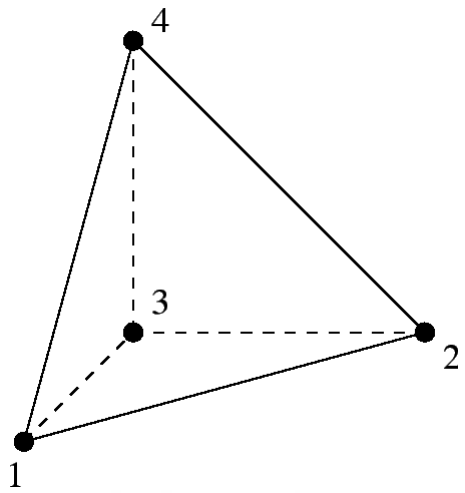


Figure 3.5. Four-noded tetrahedral element used for the simulations.

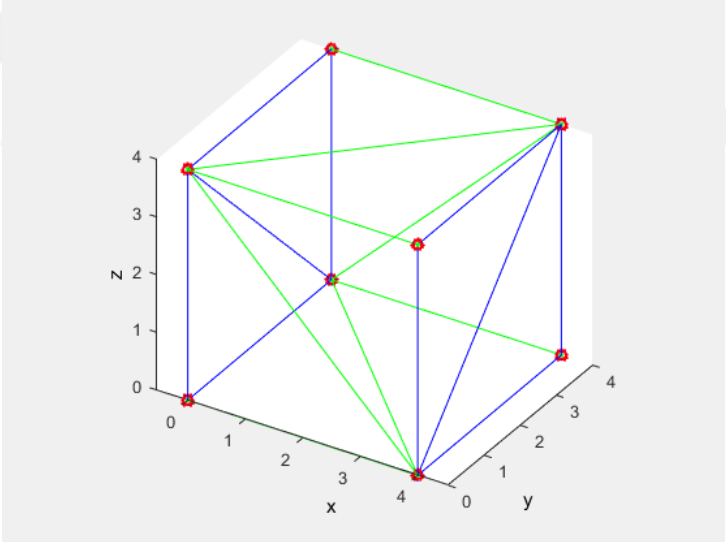


Figure 3.6. Initial condition and mesh of the sample with one element in each direction.

The applied force is released when the effective strain reaches 0.5, and the boundary conditions for this simulation phase is similar to the former conditions except that the z-displacements of the top face nodes are fixed for the latter phase. When the simulation with 150 time steps is finished, the final shape of the sample is that shown in

Figure 3.7. As expected, the sample is compressed in the $-z$ direction and is expanded in the x and y directions.

Then, the number of elements along each axis was increased to two with all other parameters remaining the same. The initial meshing of the sample is shown in Figure 3.8, and the final mesh in Figure 3.9.

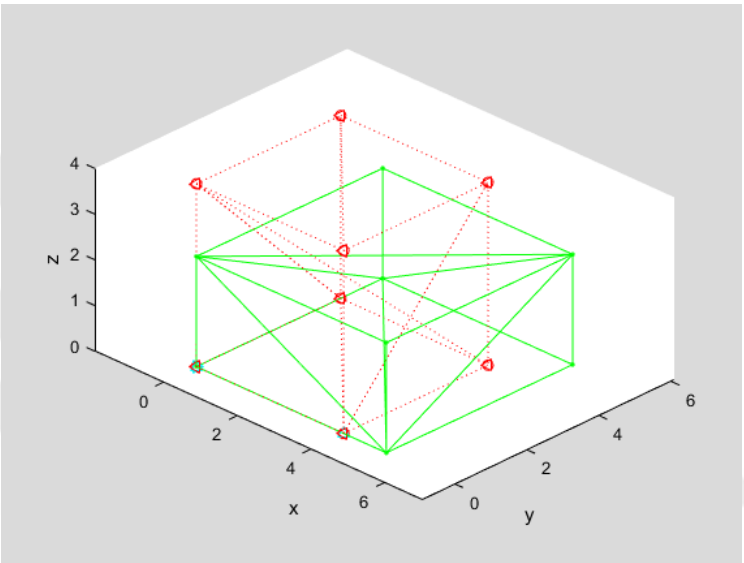


Figure 3.7. Final shape of the sample after the relaxation test with one element in each direction.

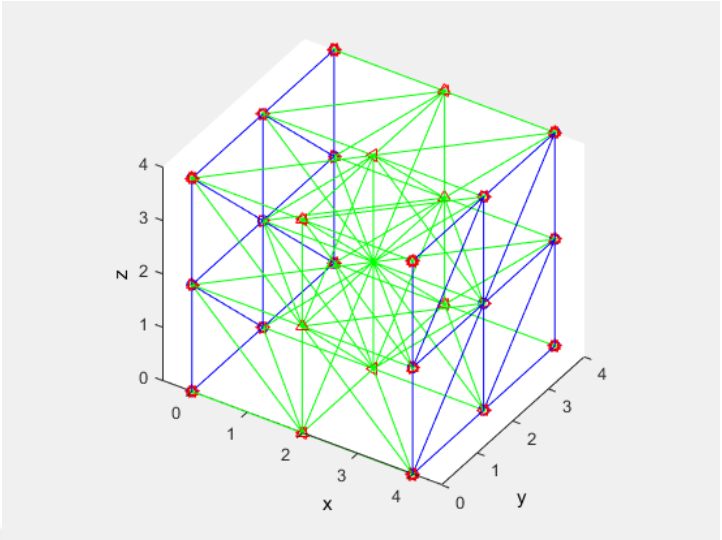


Figure 3.8. Initial condition and mesh of the sample with two elements in each direction.

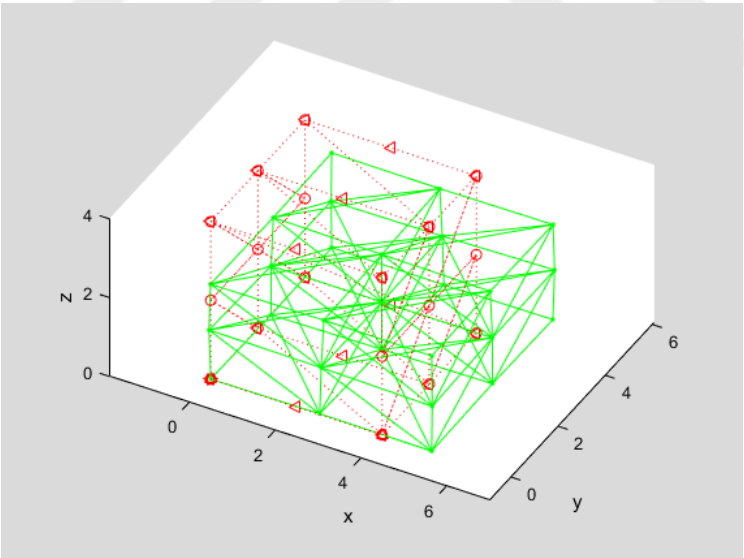


Figure 3.9. Final shape of the sample after the relaxation test with two elements in each direction.

Figure 3.10 illustrates the effect of number of elements from one to three along each axis, on the stress-time behavior, the effective stress is calculated as the Von-Mises stress. The curves indicate that the loading phase where elastic and plastic

deformations occur are the same for all three cases, and there is a small difference between the cases in the relaxation part. Further simulations are concluded with two elements per direction.

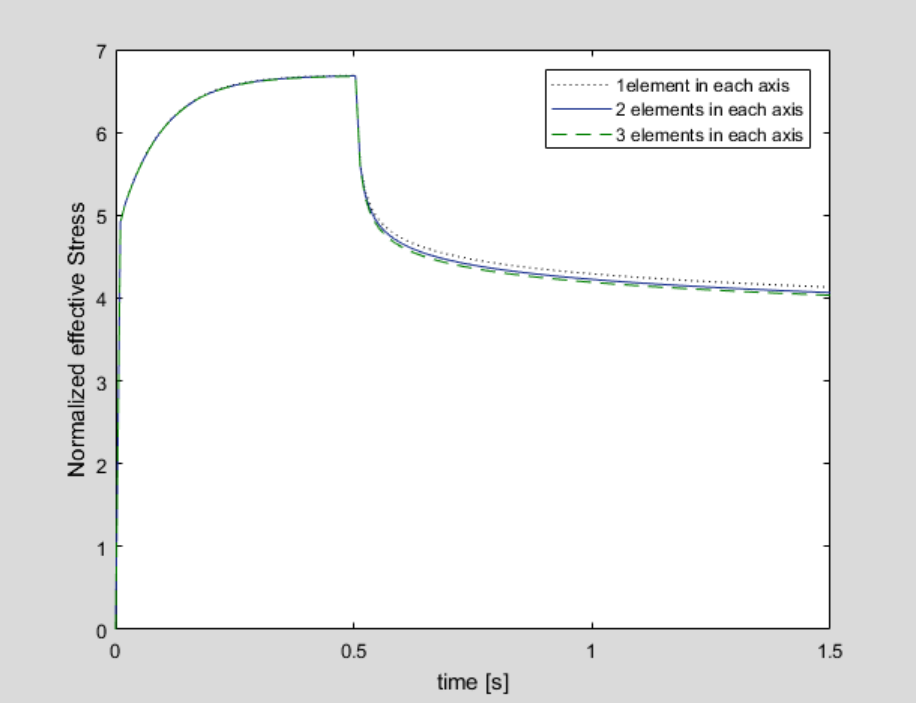


Figure 3.10. Comparison between different numbers of elements in normalized stress - time curve.

3.2.2. Investigating the Effect of Number of Time Steps in Stress Relaxation Tests

The effect of the number of time steps was then considered using 75, 150 and 300 time steps, corresponding to time increments of $\Delta t = 0.02s$, $\Delta t = 0.01s$ and $\Delta t = 0.005s$, respectively.

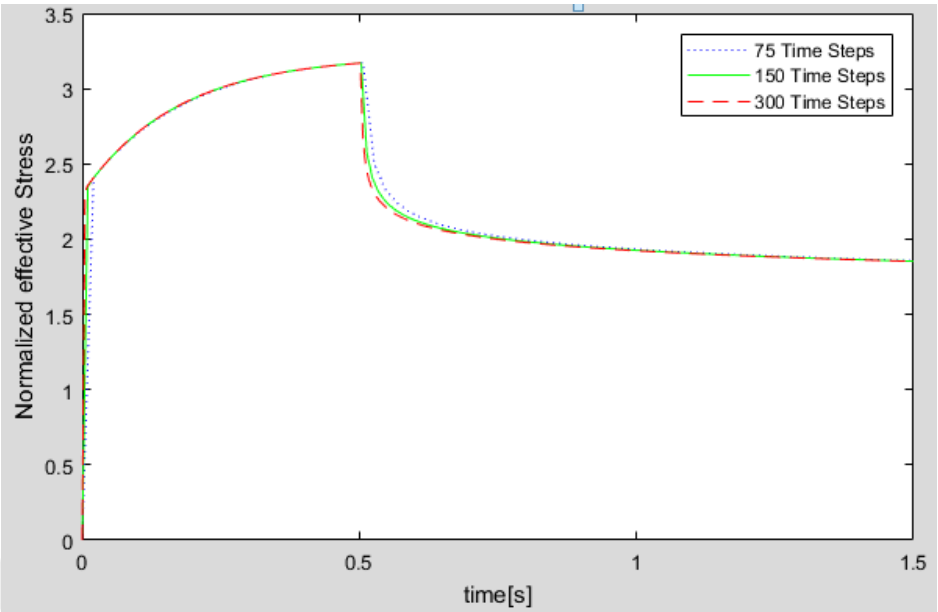


Figure 3.11. Comparison between different time steps for the normalized effective stress-time relation during the relaxation test for two elements along each axis.

We see that the results for the 3 test are nearly the same and it can be inferred that 150 time steps are sufficient. Figure 3.11 shows that the integration scheme is stable for the range of time steps which were analyzed.

3.2.3. Investigating the Effect of Compression direction on Deformation in Stress Relaxation Test

We then changed the direction of the loading from $\langle 100 \rangle$ to $\langle 110 \rangle$ in Figure 3.12 and to $\langle 111 \rangle$ in Figure 3.13. Figure 3.12 shows that when the load is applied in the $\langle 110 \rangle$ direction, the loading phase is normal but strong oscillations in the stress occur during the relaxarion phase. The probable reason for this oscillation is the non-convergence of the velocity field as shown in Figure 3.14.

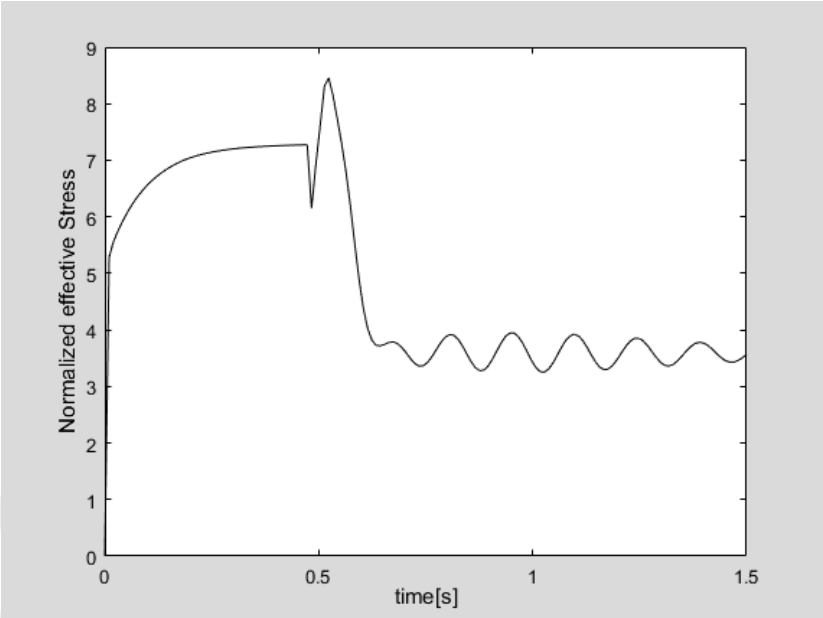


Figure 3.12. Normalized effective stress - time relation during relaxation test for two elements along each axis, 150 total time steps, and compression along the $\langle 110 \rangle$ crystal direction.

As illustrated in Figure 3.13, when the load is applied in the $\langle 111 \rangle$ direction, the elastic part seems normal, but the plastic part and the relaxation phase show unphysical behavior. This is again conjectured to be due to the non-convergence of the volumetric part of the stress and the non-convergence of the velocity field.

More fundamentally, this could be related to insufficient slip systems in the single crystal systems, since the effect is not observed when using a homogenization scheme.

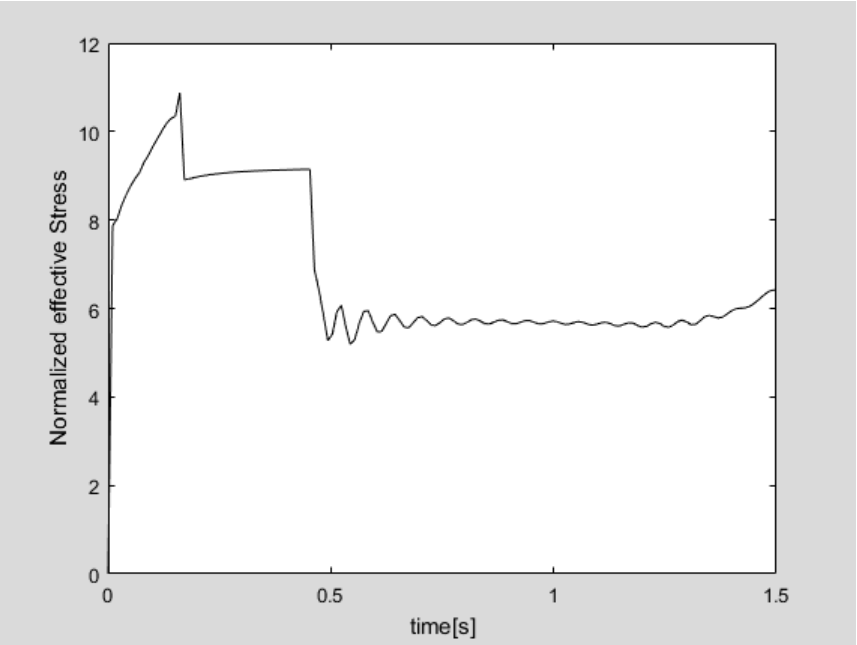


Figure 3.13. Normalized effective stress - time relation during a relaxation test with two elements along each axis, 150 total time steps, and compression along the ⟨111⟩ direction.

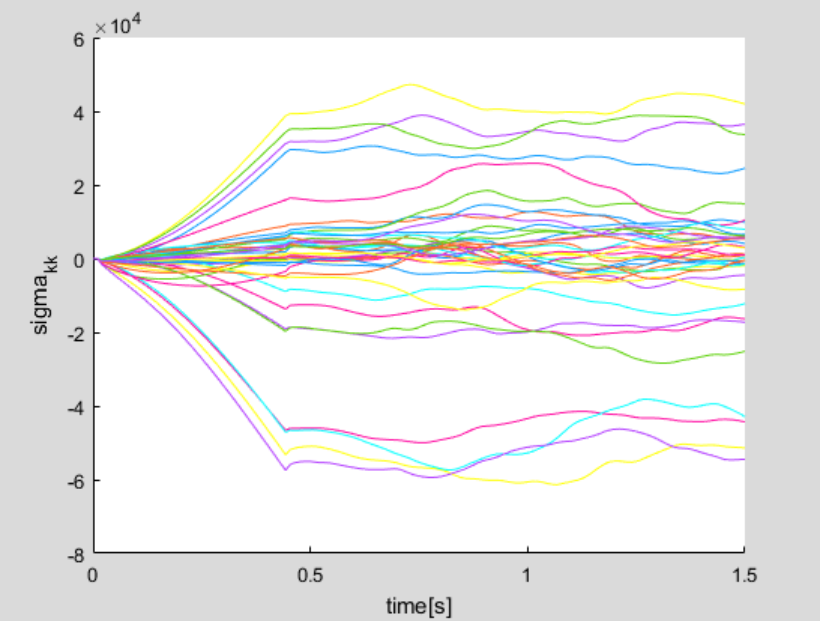


Figure 3.14. Non-convergence of the volumetric part of the stress - time curve for a single crystal in the relaxation test.

3.2.4. Polycrystal Modelling for the Relaxation Test

Although Marin and Dawson talk about modelling on the scale of single crystals in their articles [46, 47], they do not provide any single crystal results and only report results for polycrystal cases. As stated above, we believe that the main reason for the unphysical behavior is the non-convergence of the volumetric parts of the stress and strain as illustrated in Figure 3.14. This results in the non-convergence of the velocity field.

For the polycrystal cases, each element is taken as a separate crystal with a random initial orientation. A relaxation test was performed on a polycrystal with 40 crystals (elements). Figure 3.15 shows the final shape of the specimen; non-homogeneous deformation among the elements can be observed in the figure.

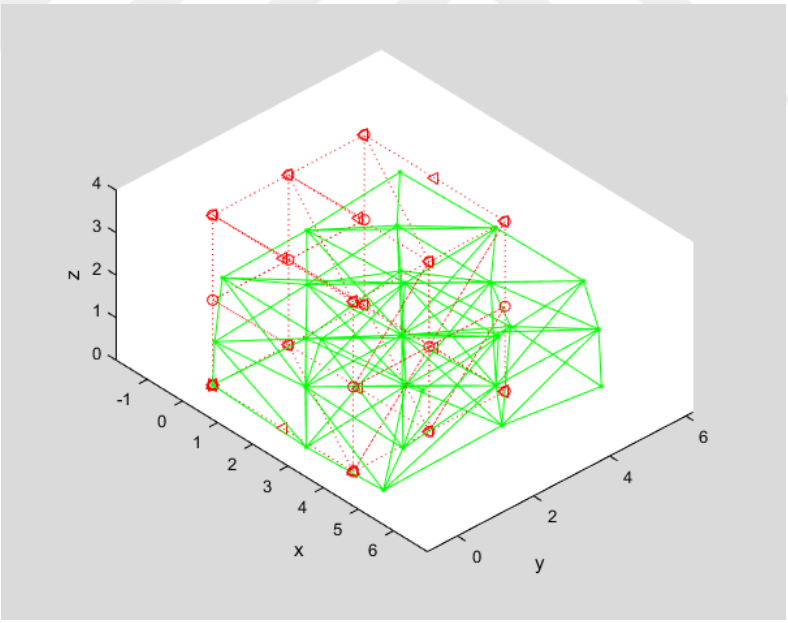


Figure 3.15. Final shape of the relaxation test for a polycrystal with 40 crystals.

Figure 3.16 represents the {100} pole figure corresponding to the random distribution of initial set of crystal orientations,. In this example the specimen is consisted of 40 tetrahedral elements where each element represents a single crystal and colored circles show the orientation of single crystals and the color bar indicated the intensity of the orientations. Figure 3.17 on the other hand, shows the pole figure for the orientations of the specimen when the effective strain reaches $\epsilon_{33} = 0.5$ and the load is removed and relaxation begins.

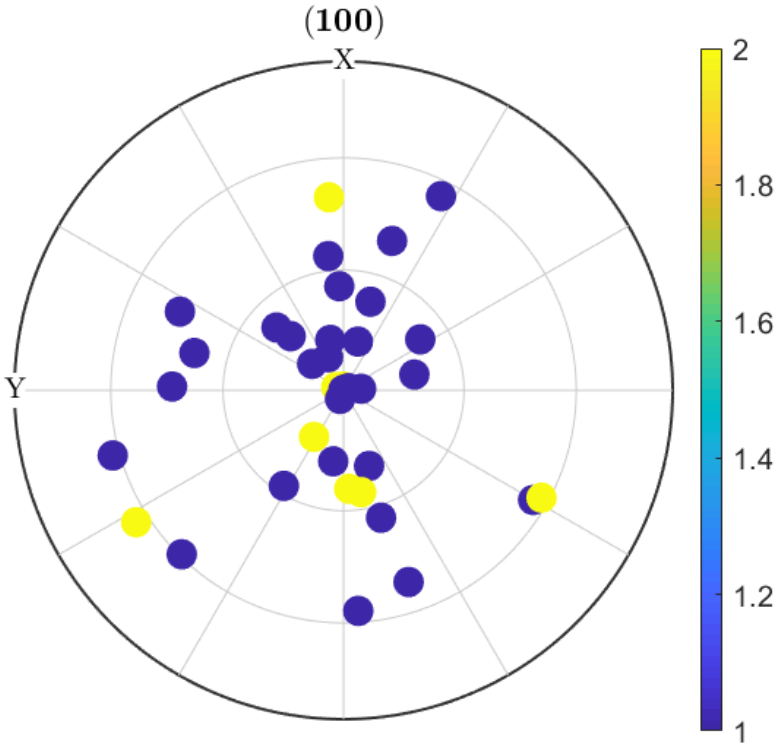


Figure 3.16. Pole figure representation of the initial crystal orientations for relaxation test.

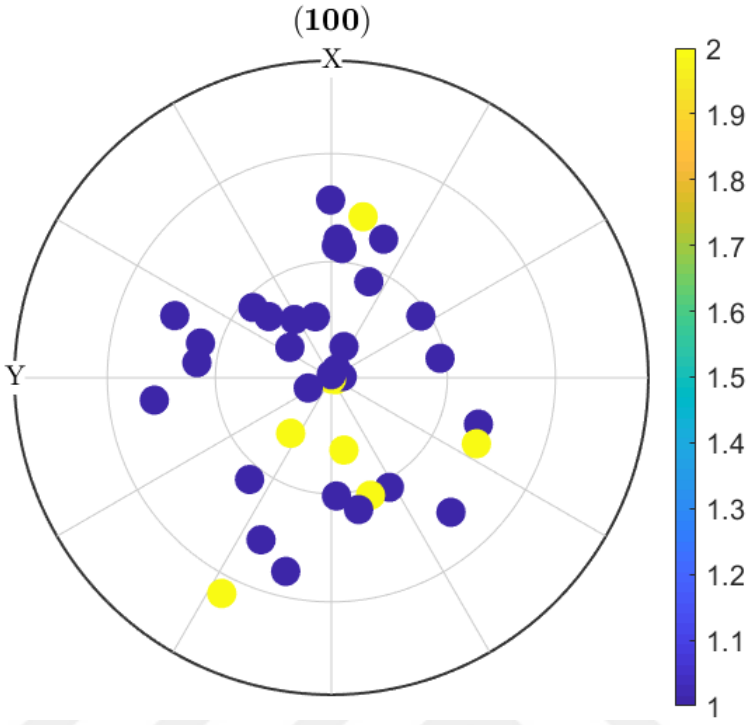


Figure 3.17. Pole figure representation of the crystal orientations before the relaxation phase.

Figure 3.18 and 3.19 illustrate the normalized effective stress - time curves for our simulation, and the corresponding result from Marin and Dawson [46] which involved 512 crystals as cubic elements. While the severe stress oscillations are absent, the simulation clearly does not perform as expected. In the model of Marin and Dawson, the deviatoric and volumetric parts are separated and because of this separation, there are not enough constraints on the volumetric part and it allows for the oscillations to take place. The non-convergence of the volumetric part can be related to the availability of the slip systems and increasing the number of elements (crystals) could possibly improve agreement with Marin and Dawson.

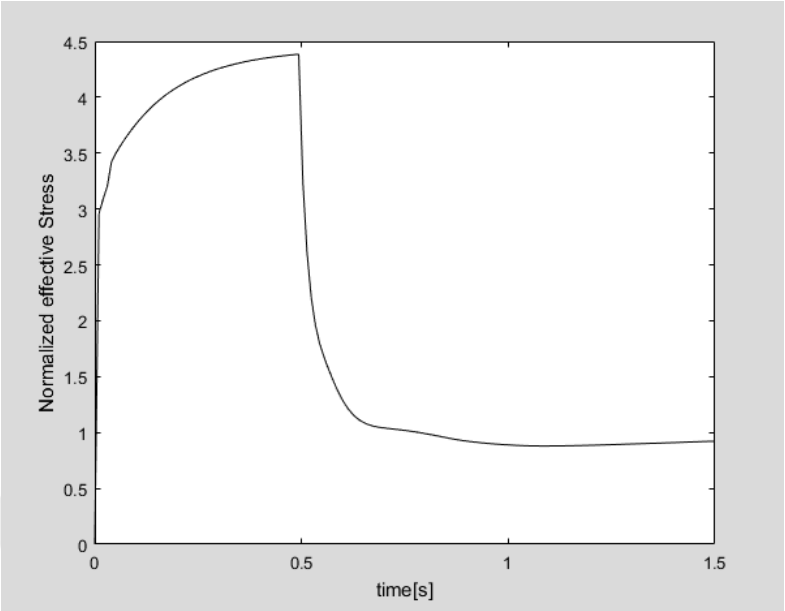


Figure 3.18. Normalized effective stress - time relation during a relaxation test for a polycrystal with 40 crystals and 150 total time steps.

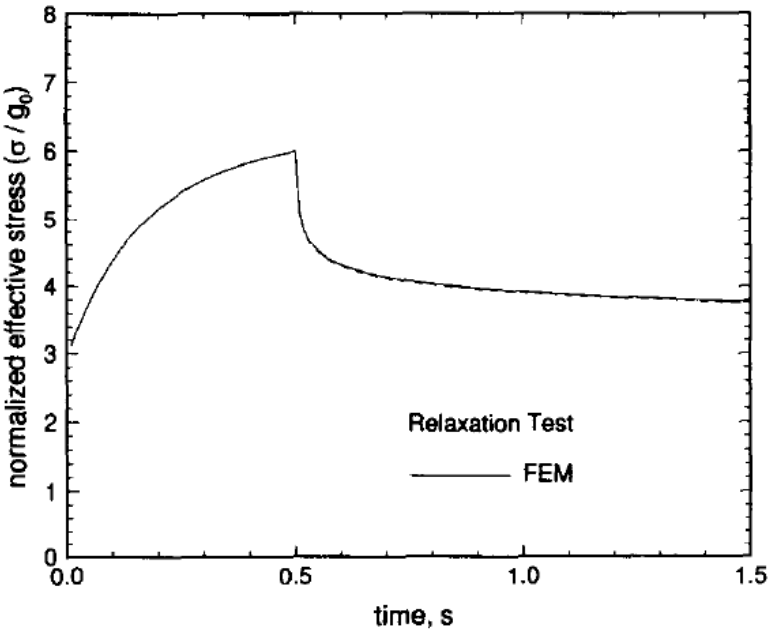


Figure 3.19. Stress - time curve for a polycrystal during a relaxation test. Reproduced from [46].

3.2.5. Reverse Loading Modelling

For reverse loading, the sample undergoes cyclic loading as tension-compression-tension. The simulation begins with application of tension in the z direction, and continues up to the point where the effective strain reaches $\epsilon_{33} = 0.5$. Up to this point, the velocity gradient is set as:

$$L = \begin{bmatrix} 0.5 & 0 & 0 \\ 0 & 0.5 & 0 \\ 0 & 0 & -1 \end{bmatrix}$$

When the strain reaches this threshold, loading direction changes to compression with the following velocity gradient:

$$L = \begin{bmatrix} -0.5 & 0 & 0 \\ 0 & -0.5 & 0 \\ 0 & 0 & 1 \end{bmatrix}$$

This compression continues on until the point where the strain reaches $\epsilon_{33} = 0.1$, when the load reverses to tension again. The boundary conditions for cyclic loading tests are similar to the boundary conditions for the relaxation test; the first node is fixed in all directions, the node corresponding to the number of nodes in the x direction is fixed in the y direction, and the nodes on the bottom face of the sample are fixed in the z direction. The final shapes of the sample under cyclic loading for one and two elements in each direction are shown in Figures 3.20 and 3.21, where the crystal is elongated in the z direction and contracted in the x and y directions.

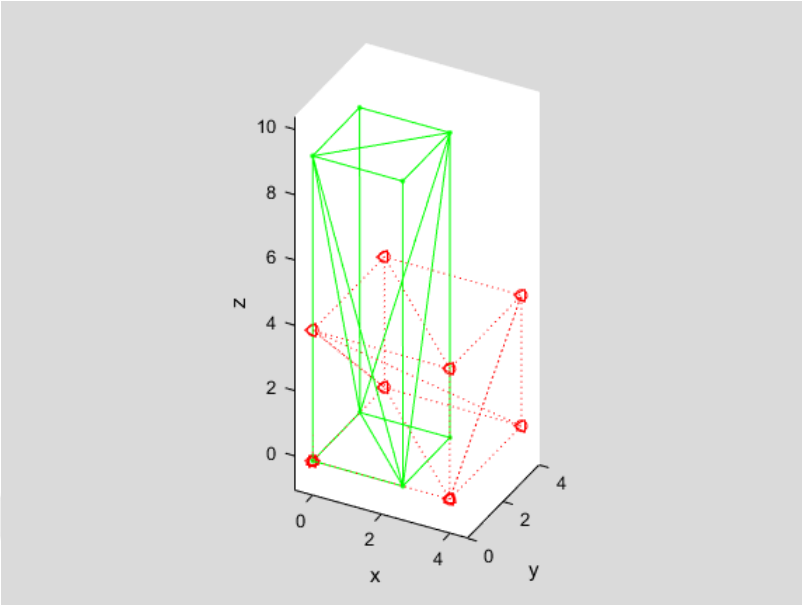


Figure 3.20. Final shape of the sample after the cyclic loading test for a single element in each direction.

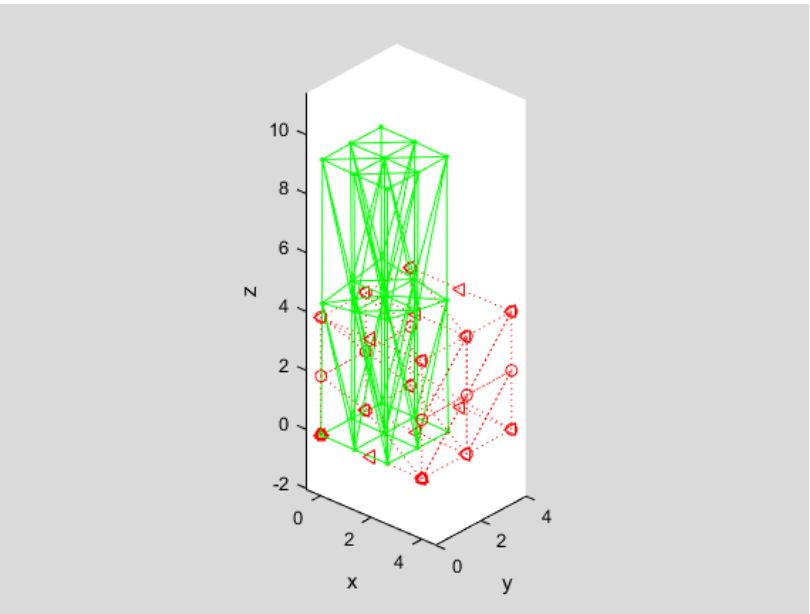


Figure 3.21. Final shape of the sample after the reverse loading test for two elements in each direction.

Figure 3.22 illustrates the stress - strain curve for the cyclic loading test for different element counts along each axis, 150 time steps, and loading along the ⟨100⟩ crystal direction. Comparing the normalized effective stress - effective strain results for different numbers of elements reveals that as the number of elements increases the hardening in the final phase increases, and in an unphysical way. This inconsistency is again attributed to the non-convergence of the stresses as shown in Figure 3.23 and increasing the number of crystals could possibly improve agreement with Marin and Dawson.

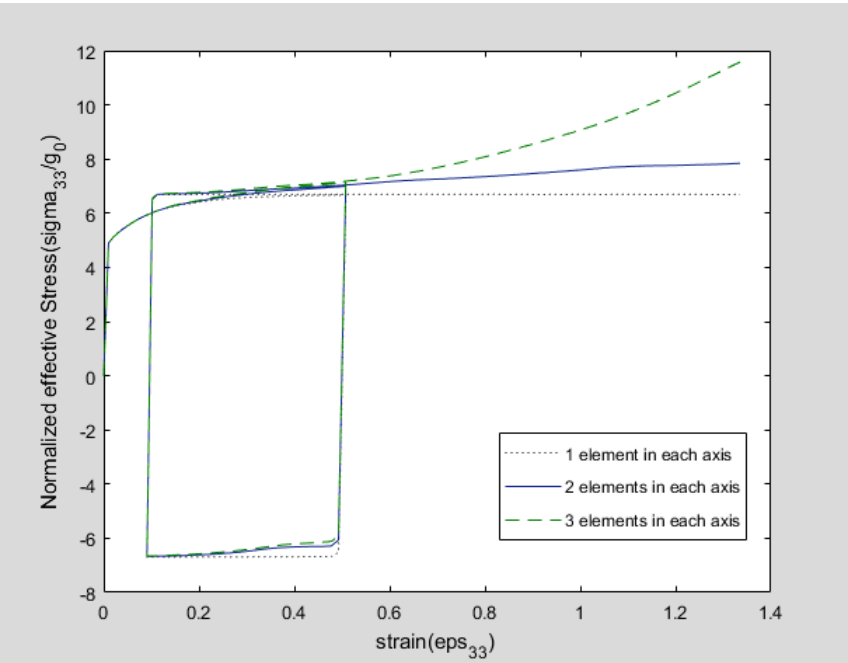


Figure 3.22. Effect of the number of elements on the stress - strain curve in the cyclic loading test.

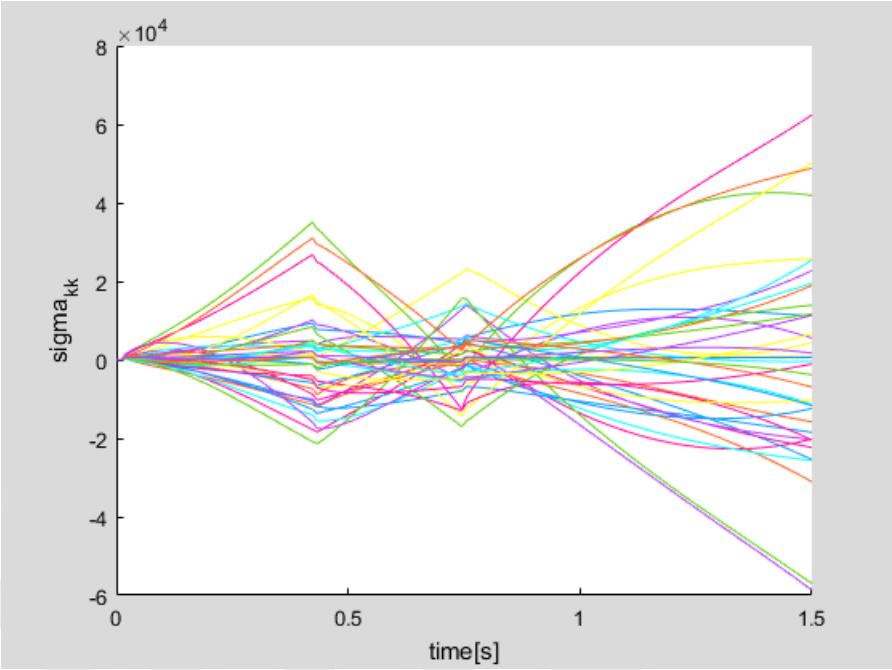


Figure 3.23. Non-convergence of the volumetric part of the stress - time curves of individual crystals in the reverse loading model.

3.2.6. Polycrystal Modelling for the Reverse Loading Test

The polycrystal model of cyclic loading is done with two elements along each axis; since each element is a single crystal, the aggregate contains 40 crystals with random initial orientations. The non-homogeneity in the deformation of elements can be observed in Figure 3.24.

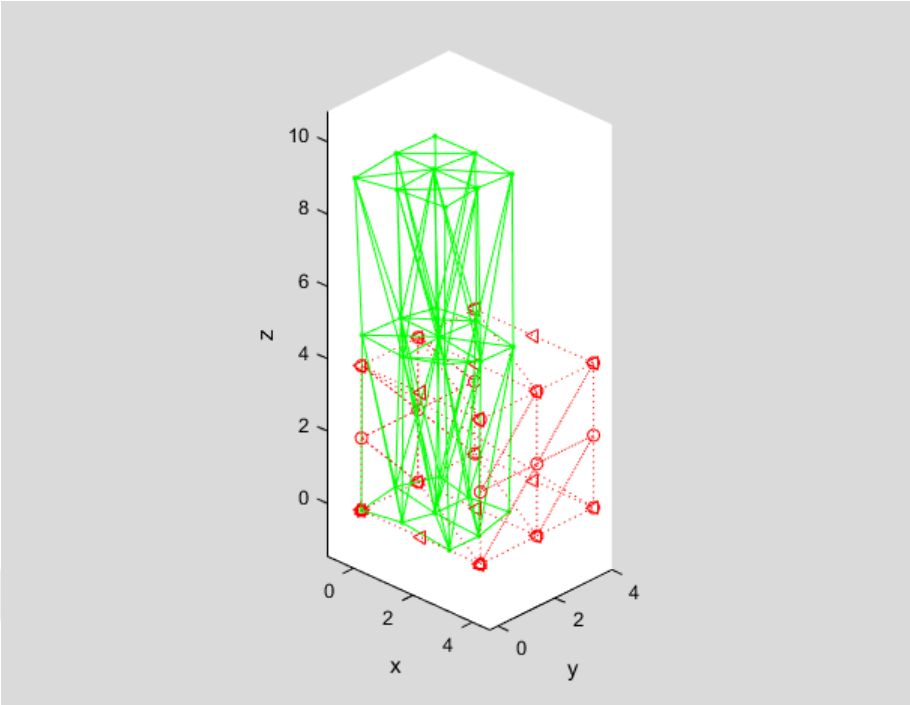


Figure 3.24. Final shape of the sample after the reverse loading test for an aggregate with 40 crystals.

Figure 3.25 illustrates the {100} pole figure representation for random initial distribution of 40 crystal orientations for the cyclic loading test, and Figures 3.26 and 3.27 represent the pole figure for the orientations of the texture when the strain reaches $\epsilon_{33} = 0.5$ and the applied tension is reversed to compression and when the effective strain reaches $\epsilon_{33} = 1$ and the applied compression changes to tension during the cyclic loading test. The orientations of the crystal are shown with colored circles and the color bar shows the intensity of the orientations.

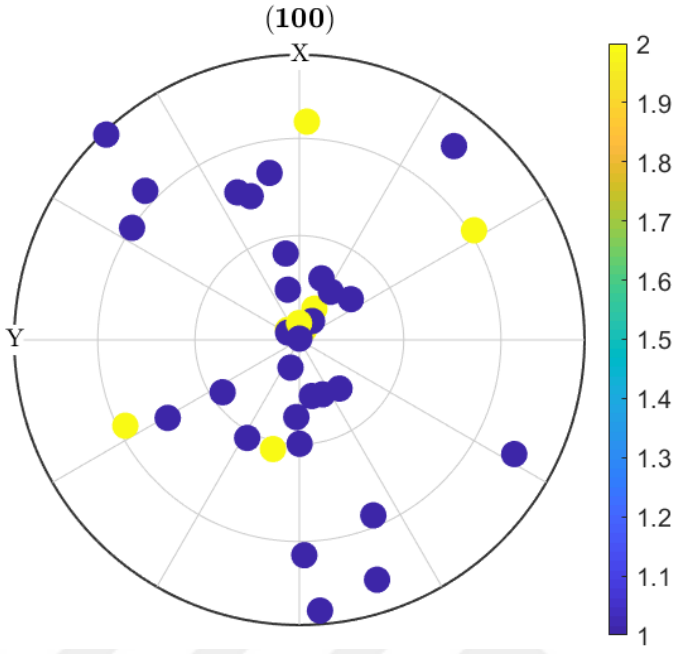


Figure 3.25. Pole figure representation of the initial crystal orientations for cyclic loading test.

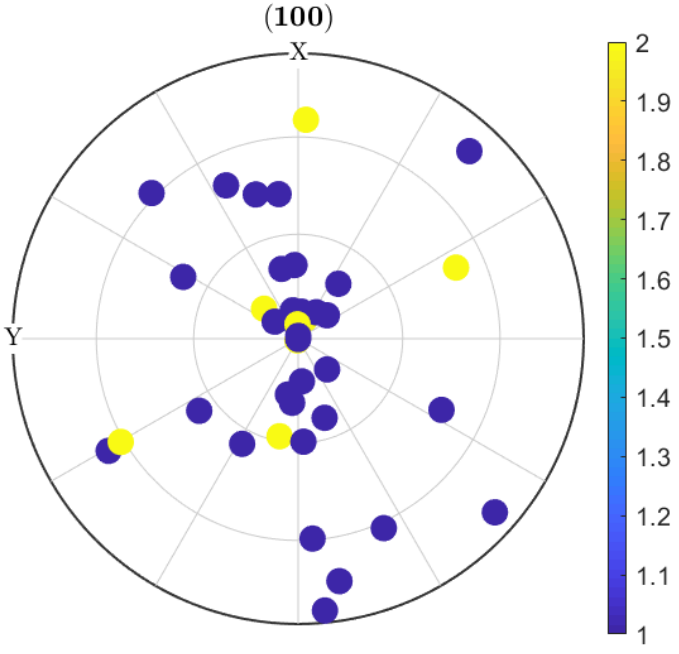


Figure 3.26. Pole figure representation of the crystal orientations when the tension is reversed to compression in the cyclic loading test.

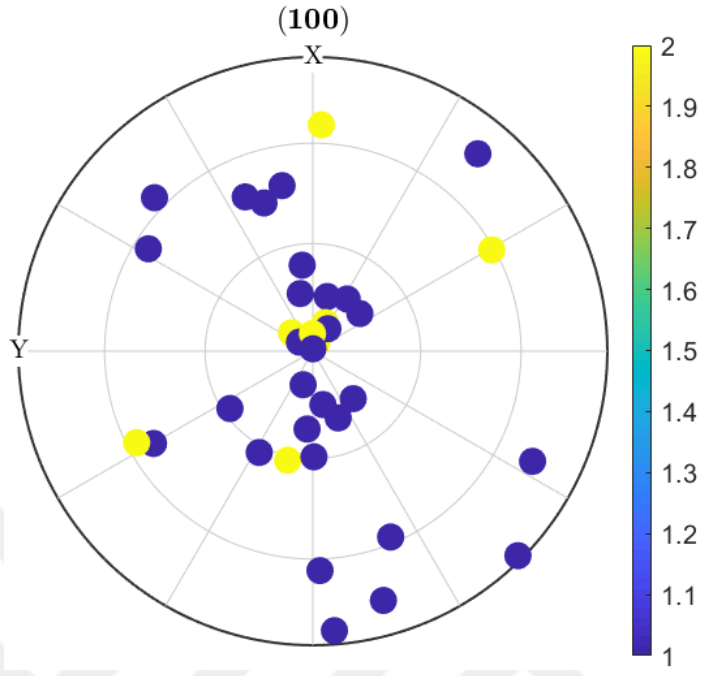


Figure 3.27. Pole figure representation of the crystal orientations when the compression is reversed to tension in the cyclic loading test.

Figures 3.25 and 3.26 compare the results of our simulations and Marin and Dawson's results. Whereas our simulation contained 40 crystals, Marin and Dawson's contained 512 crystals. As with the relaxation test, increasing the number of crystals would possibly improve the agreement.

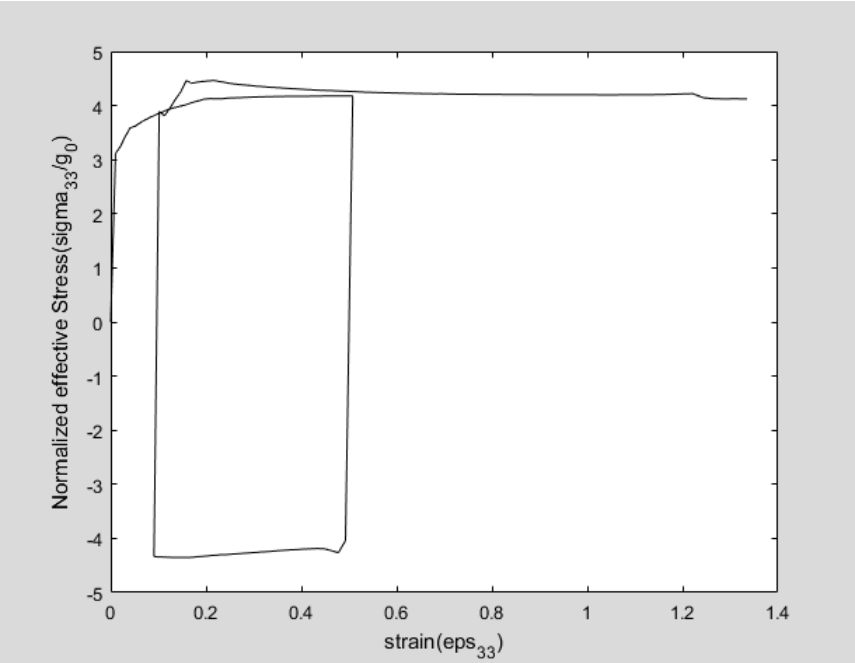


Figure 3.28. Normalized effective stress - strain curve during reverse loading test for a polycrystal with two elements along each axis and 150 total time steps.

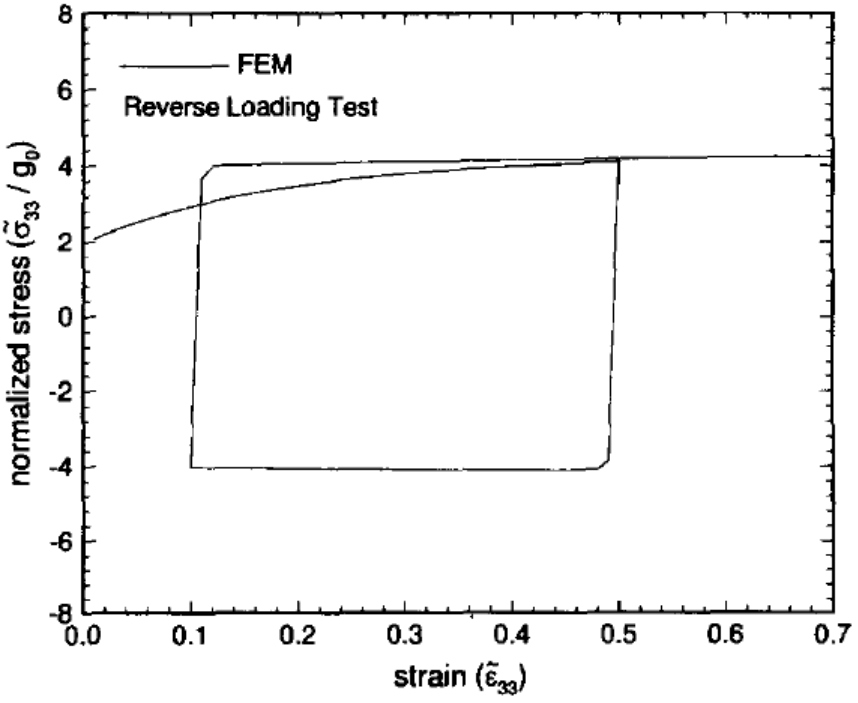


Figure 3.29. Stress - strain curve for the cyclic loading case. Reproduced from [46].

3.3. Viscoelasto-plastic deformation model (Cuitino and Ortiz's method)

The dislocation-slip based method of Cuitino and Ortiz [14] begins with the decomposition of the deformation gradient into elastic and plastic parts. The elastic deformation gradient is used to calculate the elastic right Cauchy-Green tensor $\boldsymbol{C}^e$:

$$\boldsymbol{C}^e = \boldsymbol{F}^{eT}\boldsymbol{F}^e \tag{3.51}$$

The elastic Lagrangean strain $\boldsymbol{E}^e$ is calculated from the Cauchy-Green tensor:

$$\boldsymbol{E}^e = \frac{1}{2}(\boldsymbol{C}^e - \boldsymbol{I}) \tag{3.52}$$

This leads to second Piola-Kirchhoff stress $\boldsymbol{T}^*$:

$$\boldsymbol{T}^* = \zeta \boldsymbol{E}^e \tag{3.53}$$

The total deformation gradient is calculated for all the time steps using a method similar to that Marin and Dawson used to calculate the velocity gradient. Using the total deformation gradient for the next time step and the plastic deformation from the previous iteration, the elastic deformation gradient is calculated as:

$$\boldsymbol{F}^e = \boldsymbol{F}_{n+1}\boldsymbol{F}_n^{P-1} \tag{3.54}$$

The hardening in the new time step is calculated using:

$$g_{n+1}^{\alpha} = g_n^{\alpha} + h_n^{\alpha\alpha}\dot{\gamma}_n^{\alpha}\Delta t \tag{3.55}$$

where

$$h^{\alpha\alpha} = h_c^{\alpha}\left(\frac{g^{\alpha}}{\tau_c^{\alpha}}\right)^3 \left\{ \cosh\left[\left(\frac{\tau_c^{\alpha}}{g^{\alpha}}\right)^2\right] - 1 \right\} \tag{3.56}$$

The hardening moduli matrix $h^{\alpha\beta}$ is assumed to be diagonal, the off-diagonal elements relating to cross hardening are assumed to be zero. The coefficients for the hardening moduli calculation can be obtained as:

$$h_c^\alpha = \frac{\tau_c^\alpha}{\gamma_c^\alpha} \tag{3.57}$$

$$\tau_c^\alpha = \alpha\mu b\sqrt{\pi n^\alpha} \tag{3.58}$$

$$\gamma_c^\alpha = \frac{b\rho^\alpha}{2\sqrt{n^\alpha}} \tag{3.59}$$

The forest dislocation density n^α characterizes the influence of the slip in a slip system on the hardening parameters of the other slip systems, with an interaction parameter $a^{\alpha\beta}$ given elsewhere for FCC crystals [20].

$$n^\alpha = \sum_\beta a^{\alpha\beta}\rho^\beta \tag{3.60}$$

$$\rho^\alpha = \rho_{sat}\left[1 - \left(1 - \frac{\rho_0}{\rho_{sat}}\right)e^{\gamma^\alpha/\gamma_{sat}}\right] \tag{3.61}$$

The shearing rate on slip system α can be formulated as:

$$\dot{\gamma}^\alpha = \begin{cases} \dot{\gamma}_0[(\frac{\tau^\alpha}{g^\alpha})^{\frac{1}{m}} - 1] & \text{if } \tau^\alpha > g^\alpha \\ 0 & \text{otherwise} \end{cases} \tag{3.62}$$

The resolved shear τ^α can be calculated using the second Piola-Kirchhoff stress as:

$$\tau^\alpha = (\boldsymbol{C}^e\boldsymbol{m}^\alpha)^T\boldsymbol{T}^*\boldsymbol{n}^\alpha \tag{3.63}$$

The plastic deformation gradient value is updated during the iterations for a given time step following:

$$\boldsymbol{F}_{n+1}^{p} = [\boldsymbol{I} - \sum_{\alpha} \Delta\gamma^{\alpha}(\boldsymbol{m}^{\alpha} \otimes \boldsymbol{n}^{\alpha})]^{-1} \boldsymbol{F}_{n}^{P} \tag{3.64}$$

When the change in the plastic deformation gradient is less than a defined tolerance, all values are updated using the converged value of the plastic deformation gradient. The Cauchy stress is then derived from the Second Piola-Kirchhoff stress and the deformation tensor using:

$$\boldsymbol{\sigma} = \frac{1}{|\boldsymbol{F}|} \boldsymbol{F}\boldsymbol{T}^{*}\boldsymbol{F}^{T} \tag{3.65}$$

One of the vital points of this simulation is the calculation of the finite element operators. These operators are elementally defined, and the global system is calculated by looping and integrating over the elements and scattering the elemental operators into a global system to solve the following equation:

$$\boldsymbol{K}\boldsymbol{U} = \boldsymbol{f}_{ext} - \boldsymbol{f}_{int} \tag{3.66}$$

$\boldsymbol{K}$ is the global stiffness matrix which can be calculated by the following equation:

$$\boldsymbol{K} = \int_{V_e} \boldsymbol{B}^{T}\hat{\boldsymbol{C}}\boldsymbol{B} w_i \det(\boldsymbol{J}) dV \tag{3.67}$$

where w_i is the weight factor of the integration point i, $\hat{\boldsymbol{C}}$ is the tangential stiffness matrix given elsewhere [14] and the strain field interpolation matrix $\boldsymbol{B}$ sets the relation of the nodal displacement and the strains of the elements:

$$\boldsymbol{B} = \boldsymbol{Q}\boldsymbol{H} \tag{3.68}$$

where $\boldsymbol{Q}$ is called the operator matrix:

$$\boldsymbol{Q}^T = \begin{bmatrix} \frac{\partial}{\partial x} & 0 & 0 & \frac{\partial}{\partial y} & 0 & \frac{\partial}{\partial z} \\ 0 & \frac{\partial}{\partial y} & 0 & \frac{\partial}{\partial x} & \frac{\partial}{\partial z} & 0 \\ 0 & 0 & \frac{\partial}{\partial z} & 0 & \frac{\partial}{\partial y} & \frac{\partial}{\partial x} \end{bmatrix} \tag{3.69}$$

and $\boldsymbol{H}$ is a $3 \times 3n$ displacement field interpolation matrix:

$$\boldsymbol{H} = \begin{bmatrix} h_1 & 0 & 0 & h_2 & 0 & 0 & \cdots & h_n & 0 & 0 \\ 0 & h_1 & 0 & 0 & h_2 & 0 & \cdots & 0 & h_n & 0 \\ 0 & 0 & h_1 & 0 & 0 & h_2 & \cdots & 0 & 0 & h_n \end{bmatrix} \tag{3.70}$$

$\boldsymbol{J}$ is the Jacobian matrix and defines the mapping between the parent coordinate system ξ, η, ζ and the spatial x,y,z coordinate system:

$$\boldsymbol{J} = \begin{bmatrix} \frac{\partial x}{\partial \xi} & \frac{\partial x}{\partial \eta} & \frac{\partial x}{\partial \zeta} \\ \frac{\partial y}{\partial \xi} & \frac{\partial y}{\partial \eta} & \frac{\partial y}{\partial \zeta} \\ \frac{\partial z}{\partial \xi} & \frac{\partial z}{\partial \eta} & \frac{\partial z}{\partial \zeta} \end{bmatrix} \tag{3.71}$$

The internal force can be calculated using the Cauchy $\boldsymbol{\sigma}$ stress and the $\boldsymbol{B}$ matrix:

$$\boldsymbol{f}_{int} = \int_{V_e} \boldsymbol{B}^T \boldsymbol{\sigma} w_i \det(\boldsymbol{J}) dV \tag{3.72}$$

After the calculation of stiffness matrix and force vector, the nodal displacement vector can be obtained using Equation 3.66. This procedure is repeated for all the time steps, and finally the deformation of the sample can be observed and analyzed.

4. CONCLUSION

The research presented in this thesis is concerned with the simulation of the crystal plasticity finite element method at the level of single grains and below. Three separate models were investigated, and the constitutive relations and procedures were taken into account. The first part involved the method by Kalidindi *et al.* [31] in which a fully implicit time integration scheme was used. This method is usually combined combined with a Taylor approximation for the simulation of polycrystal. A two level iteration scheme is used in this model for the calculation of the constitutive relations.

Since the method of Kalidindi includes homogenization, work continued on crystal plasticity framework of Marin and Dawson [31]. This framework is an elasto-viscoplastic model that uses a velocity-pressure finite element formulation which is consists of three levels of iteration. The implementation was tested for stress relaxation and cyclic loading cases to analyze the effects of the element number and time step length on the convergence. Both single crystal and polycrystal cases were considered.

Although a single crystal formulation is included in Marin and Dawson's article, they do not provide results for single crystal simulations. We observed non-convergence in the volumetric part of the stress and strain, resulting in non-convergence of the velocity field errors in the single crystal results.

Preliminary work was completed on Cuitino and Ortiz's method, which is a dislocation-based implicit formulation where the dislocation motion is regulated through forest dislocations [14].

5. RECOMMENDATIONS FOR FUTURE WORK

Future developments of this work include determining the active slip systems as part of the iteration procedure. Extending this method into polycrystal modelling and comparing the results with experimental cases would be beneficial.

To further improve this model, the explicit method of Kuchnicki [34] can be used. This is a modification of Cuitino and Ortiz's model that can be much much faster than the implicit method. An explicit subcycling algorithm is also introduced in Kuchnicki's article to make the integration of larger time steps possible. Application of the subcycling method is expected to substantially increase the calculation speed during the simulation.

All models considered in this thesis are dislocation based; extensions to include different mechanisms such as twinning and grain boundary sliding would be useful. Implementation of the models for BCC and HCP metals would also be interesting.

Finally, it would be a good idea to compare the results from these CPFEM models with the results from the CPFFT method and with the results obtained from experimental procedures.

REFERENCES

1. Holger Aretz and Frédéric Barlat. New convex yield functions for orthotropic metal plasticity. *International Journal of non-linear mechanics*, 51:97–111, 2013.

2. Robert J Asaro. Crystal plasticity. *Journal of applied mechanics*, 50(4b):921–934, 1983.

3. Robert J Asaro. Micromechanics of crystals and polycrystals. In *Advances in applied mechanics*, volume 23, pages 1–115. Elsevier, 1983.

4. Robert J Asaro and A Needleman. Overview no. 42 texture development and strain hardening in rate dependent polycrystals. *Acta metallurgica*, 33(6):923–953, 1985.

5. Robert J Asaro and JR Rice. Strain localization in ductile single crystals. *Journal of the Mechanics and Physics of Solids*, 25(5):309–338, 1977.

6. Venugopal Bachu and Surya R Kalidindi. On the accuracy of the predictions of texture evolution by the finite element technique for fcc polycrystals. *Materials Science and Engineering: A*, 257(1):108–117, 1998.

7. D Banabic, H Aretz, DS Comsa, and L Paraianu. An improved analytical description of orthotropy in metallic sheets. *International Journal of Plasticity*, 21(3):493–512, 2005.

8. F Barlat, JC Brem, Jeong Whan Yoon, *et al.* Plane stress yield function for aluminum alloy sheets—part 1: theory. *International Journal of Plasticity*, 19(9):1297–1319, 2003.

9. R Becker. Analysis of texture evolution in channel die compression—i. effects of grain interaction. *Acta metallurgica et materialia*, 39(6):1211–1230, 1991.

10. R Becker, JF Butler, Hsun Hu, and LA Lalli. Analysis of an aluminum single crystal with unstable initial orientation (001)[110] in channel die compression. *Metallurgical Transactions A*, 22(1):45–58, 1991.

11. Jack Chessa. Programing the finite element method with matlab. *Northwestern University*, 20(02), 2002.

12. Romain Corcolle. Comparison between different approaches in homogenization: Mean-field approach vs full-field approaches. In *COMPUMAG 2013*, page nc, 2013.

13. Richard Courant et al. Variational methods for the solution of problems of equilibrium and vibrations. *Lecture Notes in Pure and Applied Mathematics*, pages 1–1, 1994.

14. Alberto M Cuitino and Michael Ortiz. Computational modelling of single crystals. *Modelling and Simulation in Materials Science and Engineering*, 1(3):225, 1993.

15. Paul R Dawson and Donald E Boyce. Fepx–finite element polycrystals: Theory, finite element formulation, numerical implementation and illustrative examples. *arXiv preprint arXiv:1504.03296*, 2015.

16. DoITPoMS. *Slip in single crystals*, https://www.doitpoms.ac.uk/tlplib/slip/slip_geometry.php, accessed at July 2018.

17. NA Fleck and JW Hutchinson. A phenomenological theory for strain gradient effects in plasticity. *Journal of the Mechanics and Physics of Solids*, 41(12):1825–1857, 1993.

18. NA Fleck and JW Hutchinson. Strain gradient plasticity. *Advances in applied mechanics*, 33:296–361, 1997.

19. NA Fleck and JW Hutchinson. A reformulation of strain gradient plasticity. *Jour-*

nal of the Mechanics and Physics of Solids, 49(10):2245–2271, 2001.

20. P Franciosi and A Zaoui. Multislip in fcc crystals a theoretical approach compared with experimental data. *Acta Metallurgica*, 30(8):1627–1637, 1982.

21. H Gao, Y Huang, and WD Nix. Modeling plasticity at the micrometer scale. *Naturwissenschaften*, 86(11):507–515, 1999.

22. H Gao, Y Huang, WD Nix, and JW Hutchinson. Mechanism-based strain gradient plasticity—i. theory. *Journal of the Mechanics and Physics of Solids*, 47(6):1239–1263, 1999.

23. Huajian Gao and Yonggang Huang. Geometrically necessary dislocation and size-dependent plasticity. *Scripta Materialia*, 48(2):113–118, 2003.

24. SV Harren and RJ Asaro. Nonuniform deformations in polycrystals and aspects of the validity of the taylor model. *Journal of the Mechanics and Physics of Solids*, 37(2):191–232, 1989.

25. SV Harren, HE Deve, and RJ Asaro. Shear band formation in plane strain compression. *Acta Metallurgica*, 36(9):2435–2480, 1988.

26. R Hill. Generalized constitutive relations for incremental deformation of metal crystals by multislip. *Journal of the Mechanics and Physics of Solids*, 14(2):95–102, 1966.

27. R Hill and JR Rice. Constitutive analysis of elastic-plastic crystals at arbitrary strain. *Journal of the Mechanics and Physics of Solids*, 20(6):401–413, 1972.

28. Rodney Hill. A theory of the yielding and plastic flow of anisotropic metals. *Proc. R. Soc. Lond. A*, 193(1033):281–297, 1948.

29. John Woodside Hutchinson. Bounds and self-consistent estimates for creep of polycrystalline materials. *Proc. R. Soc. Lond. A*, 348(1652):101–127, 1976.

30. SR Kalidindi and L Anand. Macroscopic shape change and evolution of crystallographic texture in pre-textured fcc metals. *Journal of the Mechanics and Physics of Solids*, 42(3):459–490, 1994.

31. Surya R Kalidindi, Curt A Bronkhorst, and Lallit Anand. Crystallographic texture evolution in bulk deformation processing of fcc metals. *Journal of the Mechanics and Physics of Solids*, 40(3):537–569, 1992.

32. UF Kocks. The representation of orientations and textures. *Texture and Anisotropy: Preferred Orientations in Polycrystals and their Effect on Materials Properties. Cambridge Univeristy Press, Edinburgh Building, Cambridge, CB 2 2 RU, UK, 1998.*, pages 44–101, 1998.

33. UF Kocks and H Mecking. Physics and phenomenology of strain hardening: the fcc case. *Progress in materials science*, 48(3):171–273, 2003.

34. SN Kuchnicki, AM Cuitino, and RA Radovitzky. Efficient and robust constitutive integrators for single-crystal plasticity modeling. *International Journal of Plasticity*, 22(10):1988–2011, 2006.

35. RA Lebensohn, Y Liu, and P Ponte Castaneda. On the accuracy of the self-consistent approximation for polycrystals: comparison with full-field numerical simulations. *Acta Materialia*, 52(18):5347–5361, 2004.

36. RA Lebensohn, CN Tomé, and P Ponte Castaneda. Self-consistent modelling of the mechanical behaviour of viscoplastic polycrystals incorporating intragranular field fluctuations. *Philosophical Magazine*, 87(28):4287–4322, 2007.

37. Ricardo A Lebensohn. N-site modeling of a 3d viscoplastic polycrystal using fast fourier transform. *Acta materialia*, 49(14):2723–2737, 2001.

38. Ricardo A Lebensohn and CN Tomé. A self-consistent anisotropic approach for the simulation of plastic deformation and texture development of polycrystals:

application to zirconium alloys. *Acta metallurgica et materialia*, 41(9):2611–2624, 1993.

39. Saiyi Li, Eric Hoferlin, Albert Van Bael, Paul Van Houtte, and Cristian Teodosiu. Finite element modeling of plastic anisotropy induced by texture and strain-path change. *International Journal of Plasticity*, 19(5):647–674, 2003.

40. J Lian, F Barlat, and B Baudelet. Plastic behaviour and stretchability of sheet metals. part ii: Effect of yield surface shape on sheet forming limit. *International journal of plasticity*, 5(2):131–147, 1989.

41. Yanshan Lou and Hoon Huh. Prediction of ductile fracture for advanced high strength steel with a new criterion: Experiments and simulation. *Journal of Materials Processing Technology*, 213(8):1284–1302, 2013.

42. Yanshan Lou and Jeong Whan Yoon. Anisotropic yield function based on stress invariants for bcc and fcc metals and its extension to ductile fracture criterion. *International Journal of Plasticity*, 101:125–155, 2018.

43. Vlado A Lubarda. Constitutive theories based on the multiplicative decomposition of deformation gradient: Thermoelasticity, elastoplasticity, and biomechanics. *Applied Mechanics Reviews*, 57(2):95–108, 2004.

44. A Ma, F Roters, and D Raabe. On the consideration of interactions between dislocations and grain boundaries in crystal plasticity finite element modeling–theory, experiments, and simulations. *Acta Materialia*, 54(8):2181–2194, 2006.

45. Jean Mandel. Généralisation de la théorie de plasticité de wt koiter. *International Journal of Solids and structures*, 1(3):273–295, 1965.

46. EB Marin and PR Dawson. Elastoplastic finite element analyses of metal deformations using polycrystal constitutive models. *Computer methods in applied mechanics and engineering*, 165(1-4):23–41, 1998.

47. EB Marin and PR Dawson. On modelling the elasto-viscoplastic response of metals using polycrystal plasticity. *Computer Methods in Applied Mechanics and Engineering*, 165(1-4):1–21, 1998.

48. David P Mika and Paul R Dawson. Effects of grain interaction on deformation in polycrystals. *Materials Science and Engineering: A*, 257(1):62–76, 1998.

49. Raymond David Mindlin. Micro-structure in linear elasticity. *Archive for Rational Mechanics and Analysis*, 16(1):51–78, 1964.

50. Raymond David Mindlin. Second gradient of strain and surface-tension in linear elasticity. *International Journal of Solids and Structures*, 1(4):417–438, 1965.

51. Bahman Mirzakhani, Mohammad Taghi Salehi, Shahin Khoddam, *et al.* Investigation of dynamic and static recrystallization behavior during thermomechanical processing in a api-x70 microalloyed steel. *Journal of materials engineering and performance*, 18(8):1029, 2009.

52. A Molinari, GR Canova, and S Ahzi. A self consistent approach of the large deformation polycrystal viscoplasticity. *Acta Metallurgica*, 35(12):2983–2994, 1987.

53. A Needleman, RJ Asaro, J Lemonds, and D Peirce. Finite element analysis of crystalline solids. *Computer Methods in Applied Mechanics and Engineering*, 52(1-3):689–708, 1985.

54. Jwo Pan and James R Rice. Rate sensitivity of plastic flow and implications for yield-surface vertices. *International Journal of Solids and Structures*, 19(11):973–987, 1983.

55. D Peirce, RJ Asaro, and A Needleman. An analysis of nonuniform and localized deformation in ductile single crystals. *Acta metallurgica*, 30(6):1087–1119, 1982.

56. Daniel Peirce, Robert J Asaro, and A Needleman. Material rate dependence and

localized deformation in crystalline solids. *Acta metallurgica*, 31(12):1951–1976, 1983.

57. B Plunkett, O Cazacu, RA Lebensohn, and F Barlat. Elastic-viscoplastic anisotropic modeling of textured metals and validation using the taylor cylinder impact test. *International Journal of Plasticity*, 23(6):1001–1021, 2007.

58. B Plunkett, RA Lebensohn, O Cazacu, and F Barlat. Anisotropic yield function of hexagonal materials taking into account texture development and anisotropic hardening. *Acta Materialia*, 54(16):4159–4169, 2006.

59. A Prakash and RA Lebensohn. Simulation of micromechanical behavior of polycrystals: finite elements versus fast fourier transforms. *Modelling and Simulation in Materials Science and Engineering*, 17(6):064010, 2009.

60. James R Rice. Inelastic constitutive relations for solids: an internal-variable theory and its application to metal plasticity. *Journal of the Mechanics and Physics of Solids*, 19(6):433–455, 1971.

61. F Roters, P Eisenlohr, D Raabe, *et al.* Damask: the düsseldorf advanced material simulation kit for studying crystal plasticity using an fe based or a spectral numerical solver. *Procedia IUTAM*, 3:3–10, 2012.

62. Franz Roters, Philip Eisenlohr, Luc Hantcherli, Denny Dharmawan Tjahjanto, Thomas R Bieler, and Dierk Raabe. Overview of constitutive laws, kinematics, homogenization and multiscale methods in crystal plasticity finite-element modeling: Theory, experiments, applications. *Acta Materialia*, 58(4):1152–1211, 2010.

63. GB Sarma, B Radhakrishnan, and T Zacharia. Finite element simulations of cold deformation at the mesoscale. *Computational Materials Science*, 12(2):105–123, 1998.

64. Gorti B Sarma and Paul R Dawson. Texture predictions using a polycrystal plastic-

ity model incorporating neighbor interactions. *International Journal of Plasticity*, 12(8):1023–1054, 1996.

65. Mark S Shephard, E Seegyoung Seol, Cameron W Smith, *et al.* Methods and tools for parallel anisotropic mesh adaptation and analysis. In *VI International Conference on Adaptive Modeling and Simulation ADMOS*, 2013.

66. Geoffrey Ingram Taylor. Plastic strain in metals. *J. Inst. Metals*, 62:307–324, 1938.

67. Geoffrey Ingram Taylor and CF Elam. The plastic extension and fracture of aluminium crystals. *Proc. R. Soc. Lond. A*, 108(745):28–51, 1925.

68. Geoffrey Ingram Taylor and Constance F Elam. Bakerian lecture: The distortion of an aluminium crystal during a tensile test. *Proc. R. Soc. Lond. A*, 102(719):643–667, 1923.

69. P Van Houtte, A Van Bael, and J Winters. The incorporation of texture-based yield loci into elasto-plastic finite element programs. *Texture, Stress, and Microstructure*, 24(4):255–272, 1995.

70. Paul Van Houtte. Application of plastic potentials to strain rate sensitive and insensitive anisotropic materials. *International Journal of Plasticity*, 10(7):719–748, 1994.

71. Paul Van Houtte, Saiyi Li, Marc Seefeldt, and Laurent Delannay. Deformation texture prediction: from the taylor model to the advanced lamel model. *International Journal of Plasticity*, 21(3):589–624, 2005.

72. Paul Van Houtte, Sampath Kumar Yerra, and Albert Van Bael. The facet method: A hierarchical multilevel modelling scheme for anisotropic convex plastic potentials. *International Journal of Plasticity*, 25(2):332–360, 2009.

73. ZISU Zhao, Franz Roters, WEIMIN Mao, and Dierk Raabe. Introduction of a tex-

ture component crystal plasticity finite element method for anisotropy simulations. *Advanced Engineering Materials*, 3(12):984–990, 2001.

74. OC Zienkiewicz and YK Cheung. The finite element method in structural and continuum mechanics, 1967.

75. Olgierd Cecil Zienkiewicz, Robert Leroy Taylor, and Jian Z Zhu. The finite element method: Its basis and fundamentals: Its basis and fundamentals. *Butterworth-Heinemann*, 132:1987–1993, 2005.